

Polyakov loops and the Hosotani mechanism on the lattice

Guido Cossu^a Hisaki Hatanaka^b Yutaka Hosotani^c Jun-Ichi Noaki^a

^a*Theory Center, IPNS, High Energy Accelerator Research Organization (KEK),
Tsukuba, Ibaraki 305-0810, Japan*

^b*School of Physics, KIAS,
Seoul 130-722, Korea*

^c*Department of Physics, Osaka University,
Toyonaka, Osaka 560-0043, Japan*

E-mail: cossu@post.kek.jp, hatanaka@kias.re.kr,
hosotani@phys.sci.osaka-u.ac.jp, noaki@post.kek.jp

ABSTRACT: We explore the phase structure and symmetry breaking in four-dimensional SU(3) gauge theory with one spatial compact dimension on the lattice in the presence of fermions in the adjoint and fundamental representations with general boundary conditions. The eigenvalue phases of Polyakov loops and the associated susceptibility are measured on $16^3 \times 4$ lattice. The correspondence between the four phases found by Cossu and D'Elia and the gauge symmetry breaking by the Hosotani mechanism is established. Density plots of eigenvalue phases of the Polyakov loop in the simulations support the effective potential analysis of gauge symmetry breaking by the Hosotani mechanism at the non-perturbative level. We also investigate the case with fundamental fermions with varying boundary conditions, corresponding to imaginary chemical potentials, to observe a phase transition.

Contents

1	Introduction	1
2	Aharonov-Bohm phases in $SU(N)$ theory	3
2.1	Continuum gauge theory on $R^{d-1} \times S^1$	3
2.2	Gauge theory on the $N_x^3 \times N_y$ lattice	5
3	Symmetry breaking	7
4	Perturbative results	11
4.1	One-loop effective potential	11
4.2	Vacuum in presence of fermions	13
4.2.1	Adjoint fermions : $(N_{\text{fd}}, N_{\text{ad}}) = (0, 2)$	13
4.2.2	Fundamental fermions : $(N_{\text{fd}}, N_{\text{ad}}) = (4, 0)$	14
5	Lattice results	16
5.1	General remarks	16
5.2	Phase structure with adjoint fermions	16
5.3	Phase structure with fundamental fermions	19
5.4	Eigenvalues of the Wilson line	22
5.4.1	Weak coupling regime: fundamental and adjoint fermions	23
5.4.2	Strong coupling regime: adjoint fermion	24
6	Discussions	27
A	Useful formulas for $V_{\text{eff}}(\theta)$	28
B	Lattice technical details	29

1 Introduction

Symmetry breaking mechanisms play a central part in the unification of gauge forces. The gauge symmetry of a unified theory must be partially and spontaneously broken at low energies to describe the nature. In the standard model (SM) of electroweak interactions, the Higgs scalar field induces the symmetry breaking. There are other mechanisms of gauge symmetry breaking. In technicolor theories, strong technicolor gauge forces induce condensates of fermion-antifermion pairs in the same manner as in QCD, which in turn breaks the gauge symmetry.

In addition to these mechanism there is another intriguing scenario of dynamical gauge symmetry breaking by adding compact extra dimensions. Let us start with a gauge theory

defined in space-time with extra spatial dimensions. In brief, when the extra dimensional space is not simply-connected, the non-vanishing phases θ_H of the Wilson line integral of gauge fields along a non-contractible loop in these extra dimensions can break the symmetry of the vacuum at one loop level [1–4]. These phases θ_H are the Aharonov-Bohm (AB) phases in the extra dimensional space, which, despite its vanishing field strengths, affect physics leading to gauge symmetry breaking. This is the so called the Hosotani mechanism. The values of θ_H are determined dynamically.

These AB phases θ_H play the role of the Higgs field in the SM. Indeed, the 4D Higgs boson appears as 4D fluctuations of θ_H , or the zero-mode of the extra-dimensional component of gauge potentials A_M . This leads to a scenario of gauge-Higgs unification [5]. The 4D Higgs boson is a part of gauge fields in higher dimensions. Its mass is generated radiatively at the quantum level and turns out to be finite, free from divergences. Recently, the Hosotani mechanism has been applied to the electroweak interactions [6–18]. The gauge-Higgs unification scenario gives several predictions to be tested at LHC/ILC [19–23]. It should be pointed out, however, that the Hosotani mechanism as a mechanism of gauge symmetry breaking has been so far established only in perturbation theory. It is based on the evaluation of the effective potential $V_{\text{eff}}(\theta_H)$ at the one-loop level. It is still not clear whether the mechanism operates at the non-perturbative level. This paper is a first investigation on the non-perturbative realization of the Hosotani mechanism using lattice calculations.

Lattice QCD has been accepted as a successful non-perturbative scheme describing strong interactions. It provides a reliable method for investigating strong gauge interaction dynamics from first principles, establishing the color confinement and the chiral symmetry breaking in QCD, for example. In a recent work, Cossu and D’Elia [24] (inspired by the semi-classical study [25]) considered the case of SU(3) lattice gauge theory with fermions in the adjoint representation. They showed in a four dimensional lattice with one compact dimension (i.e. much smaller than the others in a finite volume), that the presence of periodic fermions in the adjoint representation leads to new phases in the space of the gauge coupling and fermion mass parameters. They found four different phases by measuring Polyakov loops average values. Besides the usual confined and deconfined phases, found using anti-periodic boundary condition (finite temperature), they identified two new phases, called the split and reconfined phases.

In this paper, we would like to point out the connection between the phases identified by Cossu and D’Elia and the Hosotani mechanism [26] by showing that the deconfined phase, the split phase, and the reconfined phase introduced in ref. [24] correspond to the SU(3) phase, the SU(2)×U(1) phase, and the U(1)×U(1) phase in the language of the Hosotani mechanism. Results of measurements of Polyakov loops in numerical simulations on the lattice, with fermions in the adjoint and fundamental representation, are interpreted in terms of the effective potential of the AB phases. A clear connection to the location of minima of the effective potential $V_{\text{eff}}(\theta_H)$ can be identified by the density plots of eigenvalue phases of Polyakov loops. We refine the connection by generalizing the boundary conditions for fermions in the fundamental representation, which corresponds to introducing an imaginary chemical potential. The analysis of the present paper paves the way for establishing the

Hosotani mechanism on the lattice. Once established, it can be applied to the electroweak unification and the grand unification of electroweak and strong interactions to achieve a paradigm of gauge unification without recourse to elementary scalar fields. Phase structure and the Hosotani mechanism in $SU(3)$ gauge theory, including chiral symmetry breaking, have been discussed recently [27].

The definition of a lattice gauge theory in more than 4 dimensions is afflicted with a subtle problem of finding the continuum limit. There have been many investigations in this direction [28–33]. Lattice gauge theory on orbifolds has been under intensive study for applications to electroweak interactions in mind. In this paper we take advantage of the fact that the Hosotani mechanism works in any dimensions such as $R^n \times S^1$, so we focus on the four-dimensional case ($R^3 \times S^1$) in which the lattice gauge theory has been firmly established.

The paper is organized as follows. In Section 2, after introducing the AB phases θ_H in our setup, we explain the relationship between θ_H and the Polyakov. We also briefly describe how the Polyakov loop is obtained on the lattice. Section 3 contains discussion on the gauge symmetry breaking by the Hosotani mechanism and classification of θ_H 's according to the pattern of the symmetry breaking. A perturbative prediction of θ_H is given in Sec. 4 from the analysis of the effective potential $V_{\text{eff}}(\theta_H)$ at the one loop level. The results to be compared with the lattice calculation are obtained in the presence of massless and massive fermions in the adjoint and fundamental representations with general boundary conditions. Our lattice simulations are presented in Sec. 5. In the first two sections, the simulations with adjoint fermions and fundamental fermions are discussed. We obtain the phase structures for both cases and discuss their connection to the perturbative prediction. A more direct comparison of our data to the analysis of $V_{\text{eff}}(\theta_H)$ is carried out in Sec. 5.4 in terms of eigenvalue phases of Polyakov loops (or, Wilson lines). Section 6 is devoted to discussion.

2 Aharonov-Bohm phases in $SU(N)$ theory

Let us begin the analysis by presenting the relation between the Aharonov-Bohm phases in the extra-dimensions and a relevant quantity measured in lattice gauge theory calculations: the Polyakov loop. We define these basic observables and show how we can obtain information on the Hosotani mechanism from lattice measurements.

2.1 Continuum gauge theory on $R^{d-1} \times S^1$

As the simplest realization of the Hosotani mechanism, we consider $SU(3)$ gauge theory coupled with fermions in the fundamental representation (ψ_{fd}) and/or in the adjoint representation (ψ_{ad}) in d -dimensional flat space-time with one spatial dimension compactified on S^1 [34, 35]. The circle S^1 has coordinate y with a radius R so that $y \sim y + 2\pi R$. In terms of these quantities the Lagrangian density is given by:

$$\mathcal{L} = -\frac{1}{2}\text{Tr} F_{MN}F^{MN} + \bar{\psi}_{\text{fd}}(\mathcal{D}_{\text{fd}} - m_{\text{fd}})\psi_{\text{fd}} + \text{Tr} \bar{\psi}_{\text{ad}}(\mathcal{D}_{\text{ad}} - m_{\text{ad}})\psi_{\text{ad}} \quad (2.1)$$

where \mathcal{D}_{fd} and \mathcal{D}_{ad} denote covariant Dirac operators. The gauge potentials $A_M = (A_\mu, A_y)$ ($\mu = 1, \dots, d-1$) and fermions $\psi_{\text{fd}}, \psi_{\text{ad}}$ satisfy the following boundary conditions:

$$\begin{aligned} A_M(x, y + 2\pi R) &= V A_M(x, y) V^{-1}, \\ \psi_{\text{fd}}(x, y + 2\pi R) &= e^{i\alpha_{\text{fd}}} V \psi_{\text{fd}}(x, y), \\ \psi_{\text{ad}}(x, y + 2\pi R) &= e^{i\alpha_{\text{ad}}} V \psi_{\text{ad}}(x, y) V^{-1}, \end{aligned} \quad (2.2)$$

where $V \in SU(3)$. With these boundary conditions the Lagrangian density is single-valued on S^1 , namely $\mathcal{L}(x, y + 2\pi R) = \mathcal{L}(x, y)$, so that physics is well-defined on the manifold $R^{d-1} \times S^1$. It has been proven (see [4]) that physics is independent of V at the quantum level so we adopt $V = I$ hereafter. Setting $\alpha_{\text{fd}} = \alpha_{\text{ad}} = 0$ corresponds to periodic fermions, whereas $\alpha_{\text{fd}} = \alpha_{\text{ad}} = \pi$ to anti-periodic fermions. In the Matsubara formalism of finite temperature field theory the imaginary time corresponds to S^1 with boundary conditions $\alpha_{\text{fd}} = \alpha_{\text{ad}} = \pi$. When S^1 represents a spatial dimension, α_{fd} and α_{ad} can take arbitrary values and become important in the calculation of the effective potential.

There is a residual gauge invariance given the boundary conditions (2.2). Under a gauge transformation $A'_M = \Omega A_M \Omega^{-1} + (i/g)\Omega \partial_M \Omega^{-1}$, $\psi'_{\text{fd}} = \Omega \psi_{\text{fd}}$, and $\psi'_{\text{ad}} = \Omega \psi_{\text{ad}} \Omega^{-1}$, the boundary condition (2.2) with $V = I$ is maintained, provided

$$\Omega(x, y + 2\pi R) = \Omega(x, y) . \quad (2.3)$$

The zero mode, or a constant configuration, of A_y satisfies (2.2), but it cannot be gauged away in general. To see this, consider a Wilson line integral along S^1

$$W(x) = P \exp \left(ig \int_0^{2\pi R} dy A_y(x, y) \right) , \quad (2.4)$$

which covariantly transforms under residual gauge transformations as

$$W'(x) = \Omega(x, 0) W(x) \Omega(x, 2\pi R)^{-1} = \Omega(x, 0) W(x) \Omega(x, 0)^{-1} . \quad (2.5)$$

Consequently the eigenvalues of W are gauge invariant. They are denoted as

$$\{e^{i\theta_1}, e^{i\theta_2}, e^{i\theta_3}\} \quad \text{where} \quad \sum_{j=1}^3 \theta_j = 0 \pmod{2\pi} . \quad (2.6)$$

Constant configurations of $A_y \neq 0$ with $A_\mu = 0$ yield vanishing field strengths $\langle F_{MN} \rangle = 0$, but in general give $W \neq I$, or nontrivial θ_H . This class of configurations is not gauge equivalent to $A_M = 0$. The θ_j 's are the elements of AB phase θ_H in the extra dimension. These are the dynamical degrees of freedom of the gauge fields affecting physical quantities as in the Aharonov-Bohm effect in quantum mechanics. The constant modes of A_y factorizes as

$$A_y^{\text{const}} = \frac{1}{2\pi g R} \cdot K \begin{pmatrix} \theta_1 & & \\ & \theta_2 & \\ & & \theta_3 \end{pmatrix} K^{-1} , \quad K \in SU(3) . \quad (2.7)$$

Since the gauge transformation

$$\Omega(y) = K \begin{pmatrix} e^{in_1 y/R} & & \\ & e^{in_2 y/R} & \\ & & e^{in_3 y/R} \end{pmatrix} K^{-1},$$

$$n_j : \text{an integer}, \quad \sum_j n_j = 0, \quad (2.8)$$

satisfying eq. (2.3) transforms θ_j to $\theta'_j = \theta_j + 2\pi n_j$, the periodicity of θ_j with the period 2π is encoded by the gauge invariance.

We write W_3 and W_8 to denote the Wilson line (in eq. (2.4)) for A_y^{const} and its counterpart in the adjoint representation, respectively. Accordingly, by taking trace for relevant indices, the Polyakov loop P_3 and P_8 are defined as

$$P_3 = \frac{1}{3} \text{Tr} W_3 = \frac{1}{3} \left\{ e^{i\theta_1} + e^{i\theta_2} + e^{i\theta_3} \right\}, \quad (2.9)$$

$$P_8 = \frac{1}{8} \text{Tr} W_8 = \frac{1}{4} \left\{ 1 + \cos(\theta_1 - \theta_2) + \cos(\theta_2 - \theta_3) + \cos(\theta_3 - \theta_1) \right\}. \quad (2.10)$$

As discussed in the next section, it is possible to read off the information on the non-perturbative behavior of θ_H from the Polyakov loop calculated on the lattice.

2.2 Gauge theory on the $N_x^3 \times N_y$ lattice

We carry out a non-perturbative study of SU(3) gauge theory coupled with fermions in $(R^3 \times S^1)$ by numerical simulations of a lattice gauge theory. On the $N_x^3 \times N_y$ Euclidean lattice with an isotropic lattice spacing a , we compactify the extra dimension of size N_y by imposing the appropriate boundary conditions as in (2.2), where $R = N_y a / 2\pi$. However in a lattice simulation each of the space-like directions N_x is always finite and periodic. In order for the space-time boundary conditions not to cause any finite size artifact, N_x is set to be sufficiently larger than N_y . A ratio of $N_x/N_y = 4$ is used throughout this article.

A building block of the action on the lattice is the link variable $U_{(x,y),M}$, namely the parallel transporter of the gauge field connecting (x, y) and $(x, y) + a\hat{M}$, where \hat{M} denotes the unit vector in the M -direction. Using the plaquette *i.e.* the smallest closed path in the MN plane

$$P_{(x,y),MN} = U_{(x,y)M} U_{(x,y)+\hat{M},N} U_{(x,y)+\hat{N},M}^\dagger U_{(x,y),N}^\dagger, \quad (2.11)$$

the simplest gauge action (Wilson gauge action) is written as

$$S_g[U] = \beta \sum_{x,y,M < N} \left(1 - \frac{1}{3} \text{ReTr} P_{(x,y),MN} \right), \quad (2.12)$$

where β and the bare coupling constant g_0 are related by $\beta = 6/g_0^2$. The parameter β determines the lattice spacing through the β -function [36]. Equation (2.12) reduces to the continuum action as $a \rightarrow 0$ *i.e.* $\beta \rightarrow +\infty$ by asymptotic freedom. The Dirac operator

$D_R(U; m_R a)$ for representation $R \in \{\text{fd}, \text{ad}\}$, is given as a function of U and the bare mass $m_R a$. The lattice fermion action with N_R degenerate flavors is

$$S_f[U] = \ln \det \left[D_R(U; m_R a)^\dagger D_R(U; m_R a) \right] \quad (2.13)$$

after integrating out the fermion fields and exponentiating the resulting determinant. Using the lattice action $S = S_g + S_f$, we apply the Hybrid Monte Carlo (HMC) algorithm [37, 38] for the numerical simulation to generate an ensemble of statistically independent gauge configurations distributed with the Boltzmann weight e^{-S} .

In eq. (2.13), we deal with $D_R^\dagger D_R$ instead of D_R to ensure positivity, but this doubles the number of fermions in the simulation. As for the fermion formalism on the lattice, among the several choices we choose the standard staggered type [39] which naively describes four degenerate fundamental flavors, so eight considering eq. (2.13). By separating the action of the operator between the fields whose total coordinate $x_1 + x_2 + x_3 + y$ is even or odd, D_R acquires a block structure

$$D_R = \begin{pmatrix} D_R^{(ee)} = -m_R a & D_R^{(eo)} \\ D_R^{(oe)} & D_R^{(oo)} = -m_R a \end{pmatrix}. \quad (2.14)$$

Using the relation $D_R^{(eo)\dagger} = -D_R^{(oe)}$, $D_R^\dagger D_R$ is factorized into two blocks having equivalent contribution. For $R = \text{ad}$, further factorization into the real and the imaginary parts is possible as it is a real operator. With these relations the number of simulated fermions for both representations reduces to $N_{\text{ad}} = 2$ and $N_{\text{fd}} = 4$. These are the minimal number of flavors in our simulation.

In the case of adjoint fermions, we study the phase diagram in the plane $(\beta, m_{\text{ad}} a)$ with periodic boundary conditions in the y -direction, *i.e.* $\alpha_{\text{ad}} = 0$. On the other hand, in the fundamental fermions case we generated configurations with several $(\beta, \alpha_{\text{fd}})$, fixing the bare mass to $m_{\text{fd}} a = 0.10$, where α is introduced through the boundary conditions

$$e^{-i\alpha_{\text{fd}}} U_{(x, y+N_y), 4} = U_{(x, y), 4}. \quad (2.15)$$

Among the several quantities that can be measured on the lattice, we are mainly interested in the Polyakov loop in both representations. The discretized versions of (2.9) and (2.10) are given by

$$P_3 = \frac{1}{3N_x^3} \sum_x \text{Tr} W_3^{\text{latt}}(x) = \frac{1}{3N_x^3} \sum_x \text{Tr} \prod_{y=1}^{N_y} U_{(x, y), 4}, \quad (2.16)$$

$$P_8 = \frac{1}{8N_x^3} \sum_x \text{Tr} W_8^{\text{latt}}(x) = \frac{1}{8N_x^3} \sum_x \text{Tr} \prod_{y=1}^{N_y} U_{(x, y), 4}^{(8)} \quad (2.17)$$

where $U_{(x, y), M}^{(8)}$ is the link variable in the adjoint representation

$$U_{(x, y), M}^{(8)ab} = (U_{(x, y), M}^{(8)ab})^\dagger = \frac{1}{2} \text{Tr} [\lambda^a U_{(x, y), M} \lambda^b U_{(x, y), M}^\dagger] \quad (2.18)$$

with λ^a the Gell-Mann matrices. Note that, for a real matrix $U^{(8)}$, P_8 is a real number while P_3 is complex in general.

Generally speaking, there is a potential concern about the connection between the lattice theory and the continuum theory. The continuum theory is achieved in the large $\beta = 6/g_0^2$ limit. However, to keep physical quantities fixed in reaching the continuum limit we need larger lattice volumes and smaller bare fermion masses, which is a computationally demanding task. For this reason as a starting point of our project, we restrict ourselves to the study of the parameter-dependence of the Polyakov loops in the fixed lattice volume $N_x^3 \times N_y = 16^3 \times 4$ with the constant bare mass parameters $m_{\text{ad}}a$ and $m_{\text{fd}}a$ chosen independently from β . The choice of the parameters is not intended to keep the physics constant in the $\beta \rightarrow +\infty$ limit. In other words, we obtain the phase diagram in the lattice parameter space and infer the connection to continuum theory predictions without attempting an extrapolation to the continuum limit.

3 Symmetry breaking

To see the effect of the AB phases on the spectrum of gauge bosons we expand the fields of the SU(3) gauge theory on $R^{d-1} \times S^1$ in Kaluza-Klein modes of the extra-dimension:

$$\begin{aligned} A_M(x, y) &= \frac{1}{\sqrt{2\pi R}} \sum_{n=-\infty}^{\infty} A_M^{(n)}(x) e^{iny/R}, \\ \psi_{\text{fd}}(x, y) &= \frac{1}{\sqrt{2\pi R}} \sum_{n=-\infty}^{\infty} \psi_{\text{fd}}^{(n)}(x) e^{i(n+\alpha_{\text{fd}}/2\pi)y/R}, \\ \psi_{\text{ad}}(x, y) &= \frac{1}{\sqrt{2\pi R}} \sum_{n=-\infty}^{\infty} \psi_{\text{ad}}^{(n)}(x) e^{i(n+\alpha_{\text{ad}}/2\pi)y/R}. \end{aligned} \quad (3.1)$$

The $A_M^{(0)}(x)$ fields are the zero modes in the $(d-1)$ -dimensional space-time. These lowest modes are massless at the tree level. Some of them can acquire masses at the quantum level as we are going to show. The modes $A_y^{(n)}(x)$ ($n \neq 0$) can be gauged away, but $A_y^{(0)}(x)$ cannot (see discussion in Sec. 2.1, where we have seen that the $A_y^{(0)}$ modes represent the AB phase θ_H). A different set of the elements $(\theta_1, \theta_2, \theta_3)$ leads to a different spectrum and different phase in physics.

It has been shown that on $R^{d-1} \times S^1$ one can take $K = I$ in (2.7) without loss of generality [4]. With this background, each KK mode has the following mass-squared in the $(d-1)$ -dimensional space-time.

$$\begin{aligned} A_\mu^{(n)} : \left(m_A^{(n)}\right)_{jk}^2 &= \frac{1}{R^2} \left(n + \frac{\theta_j - \theta_k}{2\pi}\right)^2, \\ \psi_{\text{fd}}^{(n)} : \left(m_{\text{fd}}^{(n)}\right)_j^2 &= \frac{1}{R^2} \left(n + \frac{\theta_j + \alpha_{\text{fd}}}{2\pi}\right)^2 + m_{\text{fd}}^2, \\ \psi_{\text{ad}}^{(n)} : \left(m_{\text{ad}}^{(n)}\right)_{jk}^2 &= \frac{1}{R^2} \left(n + \frac{\theta_j - \theta_k + \alpha_{\text{ad}}}{2\pi}\right)^2 + m_{\text{ad}}^2. \end{aligned} \quad (3.2)$$

In particular, from the gauge boson mass of the zero-mode $(m_A^{(0)})^2$, we can discuss the remaining gauge symmetry realization after the compactification. Because the mass is given by the difference $\theta_j - \theta_k$, it is classically expected that the mass spectrum becomes SU(3) asymmetric unless $\theta_1 = \theta_2 = \theta_3 \pmod{2\pi}$. However, as a dynamical degree of freedom, θ_H has quantum fluctuation. In the confined phase, these fluctuations are large enough for the SU(3) symmetry to remain intact. For a moderate gauge coupling and sufficiently small R , θ_H would take nontrivial values to break SU(3) symmetry depending on the fermion content. To determine which value of θ_H is realized at the quantum level, it is convenient to evaluate the effective potential $V_{\text{eff}}(\theta_H)$, whose global minimum is given by the vacuum expectation values (VEVs) of θ_H . In Sec. 4, we present our study of $V_{\text{eff}}(\theta_H)$ at the one-loop level and demonstrate that VEVs of θ_H are located at certain values for given fermion content. This picture is also supported by lattice simulations presented in Sec. 5.

In the rest of this section, we discuss configurations of θ_H which are relevant in the study of $V_{\text{eff}}(\theta_H)$. Besides the configuration in the confined phase, there are three classes and two regions as follows. Note that there is no intrinsic way to distinguish θ_1, θ_2 and θ_3 . All permutations of them within each configuration are equivalent.

A : SU(3) symmetric configurations

As was discussed earlier on eq. (3.2), $\theta_1 = \theta_2 = \theta_3$ leads SU(3) symmetry of the $(d-1)$ -dimensional space-time. We label the three possibilities as $A_{1,2,3}$, whose properties are

$$\begin{aligned} A_1 : \theta_H &= (0, 0, 0), & P_3 &= 1, & P_8 &= 1, \\ A_2 : \theta_H &= (\frac{2}{3}\pi, \frac{2}{3}\pi, \frac{2}{3}\pi), & P_3 &= e^{2\pi i/3}, & P_8 &= 1, \\ A_3 : \theta_H &= (-\frac{2}{3}\pi, -\frac{2}{3}\pi, -\frac{2}{3}\pi), & P_3 &= e^{-2\pi i/3}, & P_8 &= 1. \end{aligned} \quad (3.3)$$

Lattice simulations show that these kinds of configurations appear in the deconfined phase. They are realized in a system with fermions in either adjoint or fundamental representation.

B : SU(2) \times U(1) symmetric configurations

When two elements of θ_H are the same and the third one is different, zero-elements of $(m_A^{(0)})_{jk}^2$ form a 2×1 block structure, which imply that SU(3) symmetry is broken into SU(2) \times U(1) symmetry. This is realized by configurations $B_{1,2,3}$,

$$\begin{aligned} B_1 : \theta_H &= (0, \pi, \pi), & P_3 &= -\frac{1}{3}, & P_8 &= 0, \\ B_2 : \theta_H &= (\frac{2}{3}\pi, -\frac{1}{3}\pi, -\frac{1}{3}\pi), & P_3 &= \frac{1}{3}e^{-\pi i/3}, & P_8 &= 0, \\ B_3 : \theta_H &= (-\frac{2}{3}\pi, \frac{1}{3}\pi, \frac{1}{3}\pi), & P_3 &= \frac{1}{3}e^{\pi i/3}, & P_8 &= 0. \end{aligned} \quad (3.4)$$

In terms of P_3 , this configuration seems to be realized in the ‘‘split’’ phase observed in ref. [24], where a system with periodic fermions in the adjoint representation on the lattice is studied. Further discussion on the correspondence between the B phase and the split phase are presented in Sec. 5.4.

$C : U(1) \times U(1)$ symmetric configurations

If θ_1, θ_2 and θ_3 are different from each other, there are two independent massless fields in the diagonal components in $A_\mu^{(0)}$ yielding the $U(1) \times U(1)$ gauge symmetry. This situation is realized by

$$\theta_H = (0, \frac{2}{3}\pi, -\frac{2}{3}\pi), \quad P_3 = 0, \quad P_8 = -\frac{1}{8}. \quad (3.5)$$

The appearance of such a configuration is signaled by $P_3 = 0$ in a weaker gauge coupling region than the confined phase X . This is the ‘‘reconfined’’ phase found in ref. [24].

On top of X, A, B and C , there are configurations Θ which interpolate between A and B . $\Theta_{1,2,3}$ are the labels of the lines connecting A_j and B_j phases as depicted in Fig. 1. Using an intermediate parameter $-\frac{1}{3}\pi < b < \frac{1}{3}\pi$, their properties are written as

$$\begin{aligned} \Theta_1(b): \theta_H &= (-2b, b, b), & P_3 &= \frac{1}{3}(2e^{ib} + e^{-2ib}), & P_8 &= \frac{1}{2}(1 + \cos 3b), \\ \Theta_2(b): \theta_H &= (-2b, b, b) + (\frac{2}{3}\pi, \frac{2}{3}\pi, \frac{2}{3}\pi), & P_3 &= \frac{1}{3}e^{2\pi i/3}(2e^{ib} + e^{-2ib}), & P_8 &= \frac{1}{2}(1 + \cos 3b), \\ \Theta_3(b): \theta_H &= (-2b, b, b) - (\frac{2}{3}\pi, \frac{2}{3}\pi, \frac{2}{3}\pi), & P_3 &= \frac{1}{3}e^{-2\pi i/3}(2e^{ib} + e^{-2ib}), & P_8 &= \frac{1}{2}(1 + \cos 3b). \end{aligned} \quad (3.6)$$

Θ is realized when both fermions in the adjoint representation and fermions in the fundamental representation are present. That fermion content also realizes configuration $\Phi_{1,2,3}$ which interpolates between B_j and C phases, respectively. With $\frac{2}{3}\pi < c < \pi$, they are written as

$$\begin{aligned} \Phi_1(c): \theta_H &= (0, c, -c), & P_3 &= \frac{1}{3}(1 + 2\cos c), & P_8 &= \frac{1}{2}\cos c(1 + \cos c), \\ \Phi_2(c): \theta_H &= (0, c, -c) + (\frac{2}{3}\pi, \frac{2}{3}\pi, \frac{2}{3}\pi), & P_3 &= \frac{1}{3}e^{2\pi i/3}(1 + 2\cos c), & P_8 &= \frac{1}{2}\cos c(1 + \cos c), \\ \Phi_3(c): \theta_H &= (0, c, -c) - (\frac{2}{3}\pi, \frac{2}{3}\pi, \frac{2}{3}\pi), & P_3 &= \frac{1}{3}e^{-2\pi i/3}(1 + 2\cos c), & P_8 &= \frac{1}{2}\cos c(1 + \cos c). \end{aligned} \quad (3.7)$$

Figure 1 shows all relevant values of P_3 in the complex plane. (A_1, A_2, A_3) and (B_1, B_2, B_3) form Z_3 triplets. In lattice simulations one measures the VEVs of P_3 in eq. (2.16) and P_8 in eq. (2.17). The absolute value of P_3 is strongly affected by quantum fluctuations of θ_H and is reduced at strong gauge couplings. The phase of P_3 , on the other hand, is less affected by quantum fluctuations in the weak coupling regime so that transitions from one phase to another should be seen as changes in the phase of P_3 . Indeed, this is precisely what has been found in ref. [24]. The classifications of A, B, C, Θ and Φ are summarized in Table 1, where we also include the confined phase, denoted by X , in which θ_H fluctuate and take all possible values.

The Z_3 center symmetry is yet another global symmetry. If the action has this symmetry as in the pure gauge theory or only with adjoint fermions, then its spontaneous breaking is possible. The magnitude of P_3 is the order parameter in this case. This symmetry is broken in the A -phase and the B -phase while it is unbroken in the C -phase. The phases can be classified by their global $SU(3)$ and Z_3 symmetries as follows, X : ($SU(3)$ symmetric, Z_3 symmetric), A : ($SU(3)$ symmetric, Z_3 broken), B : ($SU(3)$ broken, Z_3 broken) and C : ($SU(3)$ broken, Z_3 symmetric).

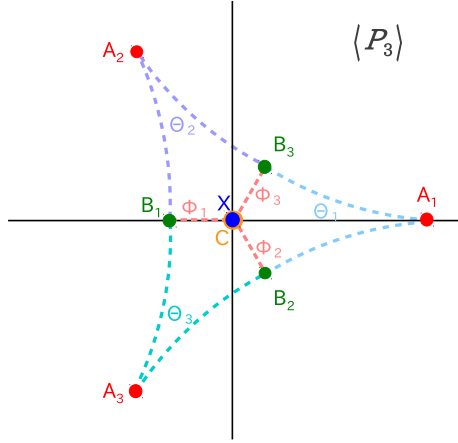


Figure 1. A sketch of the possible values of Polyakov loop in each phase. (A_1, A_2, A_3) and (B_1, B_2, B_3) form Z_3 triplets.

Table 1. Classification of the location of the global minima of $V_{\text{eff}}(\theta_H)$. In the last column the names of the corresponding phases termed in ref. [24] are also listed for X, A, B and C .

	$\theta_H = (\theta_1, \theta_2, \theta_3)$ with permutations	P_3	P_8	Global Symm., Phase
X	Large quantum fluctuations	0	$-\frac{1}{8}$	SU(3), confined
A_1 $A_{2,3}$	$(0, 0, 0)$ $(\pm\frac{2}{3}\pi, \pm\frac{2}{3}\pi, \pm\frac{2}{3}\pi)$	1 $e^{\pm 2\pi i/3}$	1	SU(3), deconfined
B_1 $B_{2,3}$	$(0, \pi, \pi)$ $(\pm\frac{2}{3}\pi, \mp\frac{1}{3}\pi, \mp\frac{1}{3}\pi)$	$-\frac{1}{3}$ $\frac{1}{3}e^{\mp\pi i/3}$	0	SU(2) \times U(1), split
C	$(0, \frac{2}{3}\pi, -\frac{2}{3}\pi)$	0	$-\frac{1}{8}$	U(1) \times U(1), reconfined
$\Theta_1(b)$ $\Theta_{2,3}(b)$	$(-2b, b, b)$ $(-2b \pm \frac{2}{3}\pi, b \pm \frac{2}{3}\pi, b \pm \frac{2}{3}\pi)$ $-\frac{1}{3}\pi < b < \frac{1}{3}\pi$	$\frac{1}{3}(2e^{ib} + e^{-2ib})$ $\frac{1}{3}e^{\pm 2\pi i/3}(2e^{ib} + e^{-2ib})$	$\frac{1}{2}(1 + \cos 3b)$	SU(2) \times U(1)
$\Phi_1(c)$ $\Phi_{2,3}(c)$	$(0, c, -c)$ $(\pm\frac{2}{3}\pi, c \pm \frac{2}{3}\pi, -c \pm \frac{2}{3}\pi)$ $\frac{2}{3}\pi < c < \pi$	$\frac{1}{3}(1 + 2\cos c)$ $\frac{1}{3}e^{\pm 2\pi i/3}(1 + 2\cos c)$	$\frac{1}{2}\cos c(1 + \cos c)$	U(1) \times U(1)

4 Perturbative results

In this section, we present the analysis on the effective potential $V_{\text{eff}}(\theta_H)$ as a function of the AB phase θ_H . The location of its global minimum defines the VEVs of $\theta_H \pmod{2\pi}$. We first give the formula for $V_{\text{eff}}(\theta_H)$ at one-loop level, and then discuss the relationship between θ_H and the Polyakov loops P_3 and P_8 .

4.1 One-loop effective potential

The first step is to separate the gauge field A_y into its vacuum expectation value $\langle A_y \rangle$ and the quantum fluctuation A_y^q . At one-loop level, the effective potential is obtained by the determinant of the logarithm of the quadratic action.

In the background gauge, which is defined by the gauge fixing

$$\begin{aligned}\mathcal{L}_{\text{gf}} &= -\frac{1}{2\alpha} \text{Tr} F[A]^2, \\ F[A] &= \partial_\mu A^\mu + ig[\langle A_\mu \rangle, A^\mu]\end{aligned}\tag{4.1}$$

and the gauge parameter $\alpha = 1$ (Feynman-'t Hooft gauge), the one-loop effective potential, after a Wick rotation, is given by

$$\begin{aligned}V_{\text{eff}}^{\text{g+gh}}(\theta_H) &= \frac{d-2}{2} \ln \det[-D_{\text{g+gh}}^2], \\ V_{\text{eff}}^{\text{R}}(\theta_H) &= -2^{\lfloor d/2 \rfloor - 1} \ln \det[-D_{\text{R}}^2],\end{aligned}\tag{4.2}$$

for the contributions coming from gauge and ghost fields and from fermions in the representation $\text{R} \in \{\text{fd}, \text{ad}\}$. $d-2$ counts the number of physical degrees of freedom of a gauge boson. $\lfloor d/2 \rfloor$ gives the largest integer which is equals to or smaller than $d/2$ and thus $2^{\lfloor d/2 \rfloor}$ counts the number of degrees of freedom of a Dirac fermion in d -dimensional space-time.

In the background configuration

$$\langle A_y \rangle = \frac{1}{2\pi Rg} \text{diag}(\theta_1, \theta_2, \theta_3), \quad \sum_{i=1}^3 \theta_i = 0,\tag{4.3}$$

the expressions for $-D_{\text{g+gh}}^2$, $-D_{\text{fd}}^2$ and $-D_{\text{ad}}^2$ are given by

$$\begin{aligned}[-D_{\text{g+gh}}^2]_{jk} &= -\partial_\mu \partial^\mu - \left[\partial_y + i \left(\frac{\theta_j - \theta_k}{2\pi R} \right) \right]^2, \\ [-D_{\text{fd}}^2]_j &= -\partial_\mu \partial^\mu - \left[\partial_y + i \left(\frac{\theta_j + \alpha_{\text{fd}}}{2\pi R} \right) \right]^2 + m_{\text{fd}}^2, \\ [-D_{\text{ad}}^2]_{jk} &= -\partial_\mu \partial^\mu - \left[\partial_y + i \left(\frac{\theta_j - \theta_k + \alpha_{\text{ad}}}{2\pi R} \right) \right]^2 + m_{\text{ad}}^2.\end{aligned}\tag{4.4}$$

Thus the one-loop effective potential becomes

$$V_{\text{eff}}(\theta_H) = V_{\text{eff}}^{\text{g+gh}}(\theta_H) + N_{\text{fd}} V_{\text{eff}}^{\text{fd}}(\theta_H) + N_{\text{ad}} V_{\text{eff}}^{\text{ad}}(\theta_H),\tag{4.5}$$

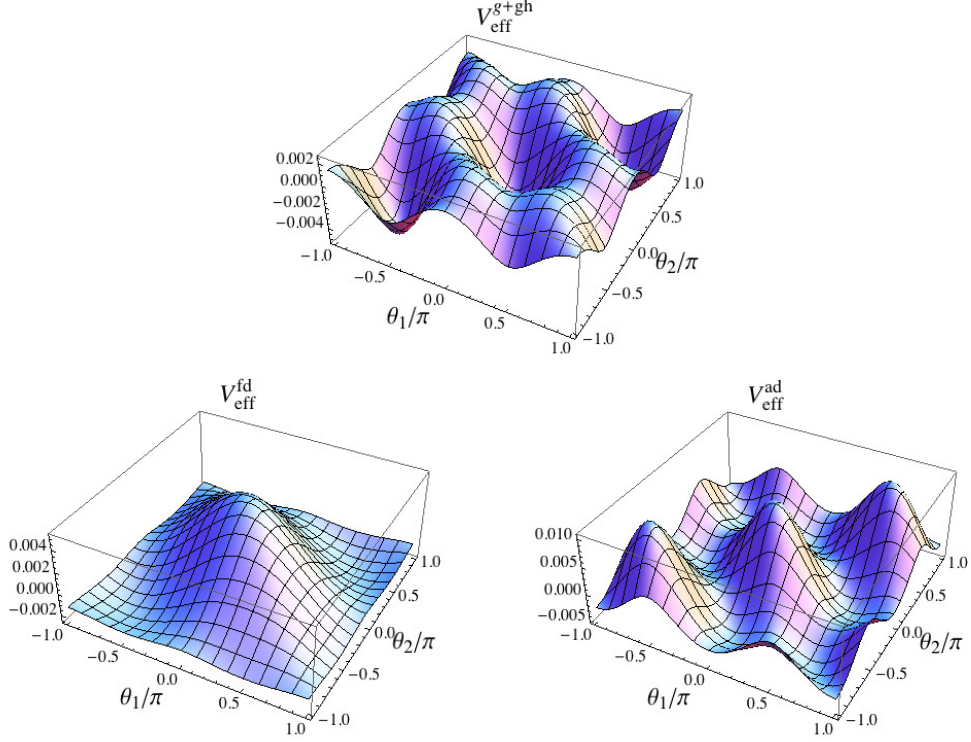


Figure 2. Three contributions to the effective potential $V_{\text{eff}}^{\text{g+gh}}(\theta_H)$, $V_{\text{eff}}^{\text{ad}}(\theta_H)$ and $V_{\text{eff}}^{\text{fd}}(\theta_H)$ are plotted for the case with $d = 4$, $m_{\text{fd}} = m_{\text{ad}} = 0$ and $\alpha_{\text{fd}} = \alpha_{\text{ad}} = 0$. R is normalized to unity.

$$\begin{aligned}
V_{\text{eff}}^{\text{g+gh}}(\theta_H) &\equiv \frac{d-2}{2} \sum_{j,k=1}^3 \sum_{n=-\infty}^{\infty} \int \frac{d^{d-1}p}{(2\pi)^{d-1}} \ln[p^2 + (m_A^{(n)})_{jk}^2], \\
V_{\text{eff}}^{\text{fd}}(\theta_H) &\equiv -2^{\lfloor d/2 \rfloor - 1} \sum_{j=1}^3 \sum_{n=-\infty}^{\infty} \int \frac{d^{d-1}p}{(2\pi)^{d-1}} \ln[p^2 + (m_{\text{fd}}^{(n)})_j^2], \\
V_{\text{eff}}^{\text{ad}}(\theta_H) &\equiv -2^{\lfloor d/2 \rfloor - 1} \sum_{j,k=1}^3 \sum_{n=-\infty}^{\infty} \int \frac{d^{d-1}p}{(2\pi)^{d-1}} \ln[p^2 + (m_{\text{ad}}^{(n)})_{jk}^2], \tag{4.6}
\end{aligned}$$

where $(m_A^{(n)})^2$, $(m_{\text{fd}}^{(n)})^2$ and $(m_{\text{ad}}^{(n)})^2$ are given in (3.2), and N_{fd} and N_{ad} are the numbers of fermions in the fundamental and adjoint representations, respectively. Note that, in eq. (4.6), both the momentum integrations and the infinite sums of KK modes yield ultraviolet (UV) divergences which are independent of θ_H and $\alpha_{\text{fd,ad}}$. Through the calculations

summarized in Appendix A, we obtain expressions of each contribution

$$\begin{aligned}
V_{\text{eff}}^{\text{g+gh}}(\theta_H) &= (d-2) \sum_{j,k=1}^3 V(\theta_j - \theta_k, 0), \\
V_{\text{eff}}^{\text{fd}}(\theta_H) &= -2^{\lfloor d/2 \rfloor} \sum_{j=1}^3 V(\theta_j + \alpha_{\text{fd}}, m_{\text{fd}}), \\
V_{\text{eff}}^{\text{ad}}(\theta_H) &= -2^{\lfloor d/2 \rfloor} \sum_{j,k=1}^3 V(\theta_j - \theta_k + \alpha_{\text{ad}}, m_{\text{ad}}),
\end{aligned} \tag{4.7}$$

where

$$\begin{aligned}
V(\theta, m) &= -\frac{\Gamma(d/2)}{\pi^{d/2}(2\pi R)^{d-1}} \sum_{n=1}^{\infty} \frac{\cos n\theta - 1}{n^d} B_{d/2}(2\pi n R m), \\
B_{d/2}(x) &\equiv \frac{x^{d/2} K_{d/2}(x)}{2^{\frac{d}{2}-1} \Gamma(d/2)}, \quad B_{d/2}(0) = 1,
\end{aligned} \tag{4.8}$$

and $K_{d/2}(x)$ is the modified Bessel function of the second kind.

In Fig. 2, $V_{\text{eff}}^{\text{g+gh}}(\theta_H)$, $V_{\text{eff}}^{\text{ad}}(\theta_H)$ and $V_{\text{eff}}^{\text{fd}}(\theta_H)$ are plotted for $m_{\text{fd}} = m_{\text{ad}} = 0$ and $\alpha_{\text{ad}} = \alpha_{\text{fd}} = 0$. In this case, $V_{\text{eff}}^{\text{g+gh}}(\theta_H)$ has degenerate global minima at $A_{1,2,3}$, reflecting the Z_3 symmetry. On the other hand, $V_{\text{eff}}^{\text{fd}}(\theta_H)$ has degenerate global minima at A_2 and A_3 while $V_{\text{eff}}^{\text{ad}}(\theta_H)$ has global minima at C , *i.e.* at the all permutations of $(0, \frac{2}{3}\pi, -\frac{2}{3}\pi)$.

4.2 Vacuum in presence of fermions

In the presence of fermions, $V_{\text{eff}}(\theta_H)$ exhibits a rich structure. Let us consider a model with $N_{\text{fd}}(N_{\text{ad}})$ fundamental (adjoint) fermions which is described by eq. (4.5). For simplicity, we restrict ourselves to the case where $m_{\text{fd}} = m_{\text{ad}}$ and $\alpha_{\text{fd}} = \alpha_{\text{ad}}$. As explained in Sec. 2.2, $N_{\text{fd}} = 4$ and $N_{\text{ad}} = 2$ are the minimal numbers of flavors for the standard staggered formalism for the lattice fermion. Therefore, in the following we briefly summarize the behavior of $V_{\text{eff}}(\theta_H)$ for $(N_{\text{fd}}, N_{\text{ad}}) = (0, 2)$ and $(4, 0)$.

4.2.1 Adjoint fermions : $(N_{\text{fd}}, N_{\text{ad}}) = (0, 2)$

Let us begin with the case of adjoint fermions under the periodic boundary condition $\alpha_{\text{ad}} = 0$. At one-loop level, $V_{\text{eff}}(\theta_H)$ depends on the mass in the product $m_{\text{ad}}R$. The global minimum of $V_{\text{eff}}(\theta_H)$ changes position according to the following pattern:

$$\begin{aligned}
&A_{1,2,3} \text{ for } 0.499 \leq m_{\text{ad}}R, \\
&B_{1,2,3} \text{ for } 0.421 \leq m_{\text{ad}}R \leq 0.499, \\
&C \text{ for } 0 \leq m_{\text{ad}}R \leq 0.421.
\end{aligned} \tag{4.9}$$

The fact that there are coexisting phases A and B (B and C) at the transition point $m_{\text{ad}}R = 0.421(0.499)$ implies that the transition is of first order.

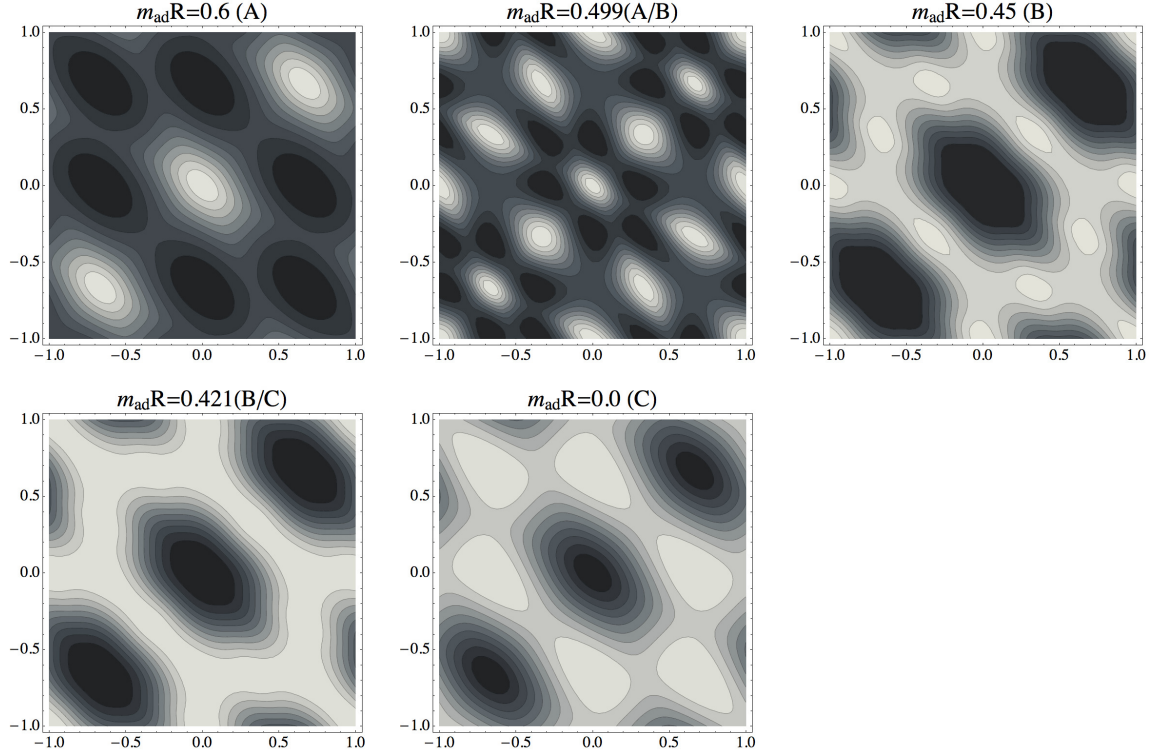


Figure 3. Effective potential for the case of $N_{\text{ad}} = 2$ adjoint fermion with periodic boundary condition ($\alpha_{\text{ad}} = 0$) for the values of $m_{\text{ad}}R$ in $d = 4$. They are corresponding to the X phase, the A - B transition point, the B phase, the B - C transition point and the C phase, respectively. Lower values of V_{eff} are indicated by lighter colors.

In Fig. 3, contour plots of $V_{\text{eff}}(\theta_H)$ are displayed in the order $m_{\text{ad}}R$ is decreasing to cover the phases A , B and C and transitions A - B and B - C according to eq. (4.9). One notes that the A - B transition is more prominent than the B - C transition because the barrier separating two minima in the potential is much higher for the former.

We find that the location of the global minimum depends on the value of α_{ad} as well. In particular, for $\alpha_{\text{ad}} = \pi$, the effective potential is identical to that at finite temperature $T = (2\pi R)^{-1}$ and the $SU(3)$ symmetry remains unbroken. For massless fermions $m_{\text{ad}} = 0$, the global minima of the effective potential are located at

$$\begin{aligned}
 &A_{1,2,3} \text{ for } 0.416\pi \leq |\alpha_{\text{ad}}| \leq \pi, \\
 &B_{1,2,3} \text{ for } 0.319\pi \leq |\alpha_{\text{ad}}| \leq 0.416\pi, \\
 &C \text{ for } |\alpha_{\text{ad}}| \leq 0.319\pi.
 \end{aligned} \tag{4.10}$$

4.2.2 Fundamental fermions : $(N_{\text{fd}}, N_{\text{ad}}) = (4, 0)$

In the presence of the fundamental fermions, the global Z_3 symmetry

$$\theta_j \rightarrow \theta_j + \frac{2}{3}\pi, \quad j = 1, 2, 3. \tag{4.11}$$

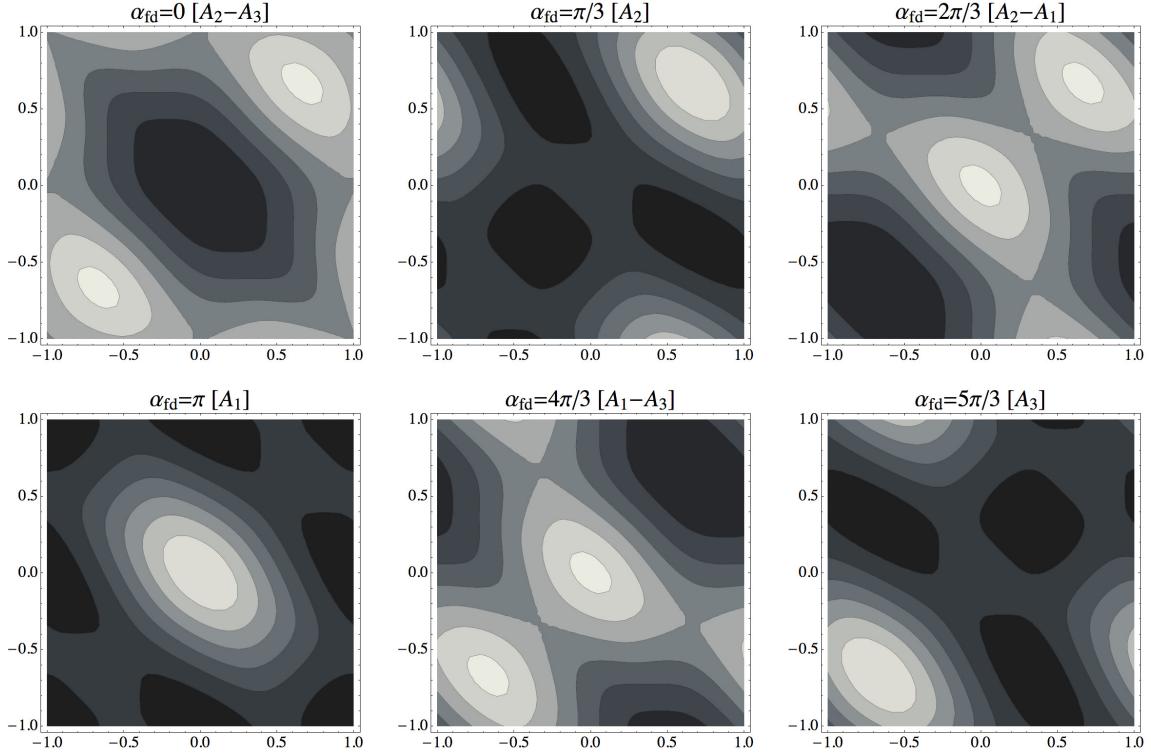


Figure 4. The effective potential with four massless fundamental fermions in the $(\theta_1/\pi, \theta_2/\pi)$ plane. Boundary condition of the fermions are changed from $\alpha_{\text{fd}} = 0$ to $\alpha_{\text{fd}} = 5\pi/3$. We plot the three phase transitions A_2 - A_3 , A_2 - A_1 and A_1 - A_3 , and three phases A_1 , A_2 and A_3 . Lower values of V_{eff} are indicated by lighter colors.

is broken. The boundary condition parameter α_{fd} plays the role of selecting one of the Z_3 related minima. We find that the fermion mass m_{fd} , on the other hand, has only a small effect on the location of the global minimum unless $m_{\text{fd}}R$ is large enough for the effect of fermions to be negligible. Contour plots of $V_{\text{eff}}(\theta_H)$ with $d = 4$ and $N_{\text{fd}} = 4$ are displayed for various values of α_{fd} in Fig. 4. The global minimum is found at

$$\begin{aligned}
 A_2 & \text{ for } 0 \leq \alpha_{\text{fd}} \leq \frac{2\pi}{3} , \\
 A_1 & \text{ for } \frac{2\pi}{3} \leq \alpha_{\text{fd}} \leq \frac{4\pi}{3} , \\
 A_3 & \text{ for } \frac{4\pi}{3} \leq \alpha_{\text{fd}} \leq 2\pi .
 \end{aligned} \tag{4.12}$$

Therefore, the phase changes $A_2 \rightarrow A_1 \rightarrow A_3 \rightarrow A_2$ as α_{fd} increases from 0 to 2π . In Fig. 5, we plot the corresponding $V_{\text{eff}}(\theta_H)$ a function of α_{fd} for two different values of $m_{\text{fd}}R$. One observes that the line of global minima has a period of $2\pi/3$ and non-analyticity at $\alpha_{\text{fd}} = 2n\pi/3$, ($n = 0, 1, 2, \dots$). This is known as Roberge-Weiss phase structure [40] which we discuss in Sec. 5.3.

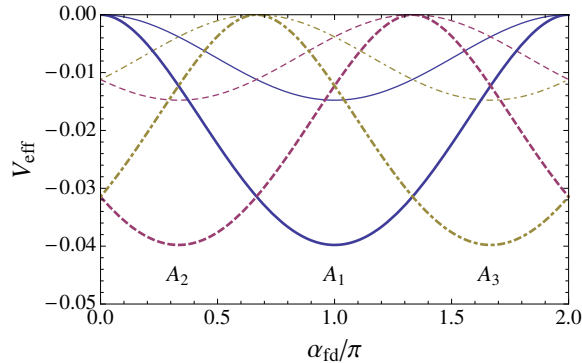


Figure 5. V_{eff} for $(N_{\text{fd}}, N_{\text{ad}}) = (4, 0)$ versus α_{fd} . Solid, dashed and dot-dashed lines correspond to values at A_1 , A_2 and A_3 , respectively. Thick [thin] lines are for $m_{\text{fd}} = 0$ [$m_{\text{fd}}R = 0.4$].

5 Lattice results

Following the general remarks in Sec. 5.1, we present our lattice study with the adjoint (fundamental) fermions in Secs. 5.2 (5.3). We separately discuss, in Sec. 5.4, the connection to the perturbative prediction by the analysis of the eigenvalue distribution.

5.1 General remarks

We compute Polyakov loops P_3 and P_8 on the $16^3 \times 4$ volume gauge configurations sampled with the weight $e^{-S_g - S_f}$, where the lattice actions S_g and S_f are given in eqs. (2.12) and (2.13), respectively. The VEV is obtained as the ensemble average of the data for finite number of configurations with a statistical error. By comparing the distribution of P_3 on the complex plane and Fig. 1, one can distinguish which phase is realized. This qualitative analysis is also done in comparing the eigenvalue distribution and the vacua (Figs. 3 and 5) obtained from the perturbative analysis. To determine the transition points, a useful quantity is the susceptibility

$$\chi_{\Omega} = N_x^3 (\langle \Omega^2 \rangle - \langle \Omega \rangle^2) \quad (5.1)$$

of the observable $\Omega \in \{|P_3|, P_8\}$ which scales with the lattice volume at the phase transitions. In connection to the perturbative results, where the relevant parameter is $m_{\text{fd}}R$ or $m_{\text{ad}}R$, increasing β has the effect of decreasing those parameters, due to the running of the renormalized fermion mass in the lattice unit. We estimate statistical errors by employing the jackknife method with appropriate bin sizes to incorporate any auto-correlations.

5.2 Phase structure with adjoint fermions

In the numerical simulation for $(N_{\text{ad}}, N_{\text{fd}}) = (2, 0)$, we use bare masses $m_{\text{ad}}a = ma = 0.05$ and 0.10 changing β covering the range $5.3 \leq \beta \leq 6.5$. Periodic boundary condition is used ($\alpha_{\text{ad}} = 0$) in the compact direction, which is different from the case with anti-periodic boundary conditions (finite temperature) where only the confined and deconfined phases are realized [41]. The essentially same setup is included in the study of ref. [24]. To explore the phase structure in heavier mass region, we also examine bare masses $m_{\text{ad}}a = ma = 0.50$

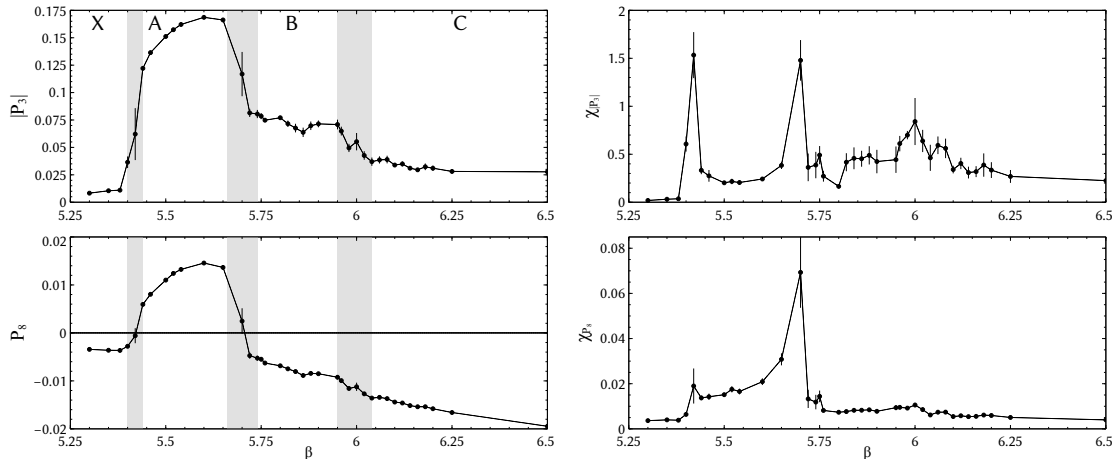


Figure 6. Left: β -dependences of $|P_3|$ (upper) and P_8 (lower). The gray bands indicate the transition regions as listed in Table 2. Each phase is labeled in the upper panel, accordingly. Right: susceptibilities corresponding to the light panels. Results for $ma = 0.10$ are shown.

and 0.80 for the range of $5.5 \leq \beta \leq 9.8$ and $5.5 \leq \beta \leq 20.0$, respectively. As will be discussed, data with those masses require even more careful treatment.

For each ma , after checking rough phase structure from the distribution plot of P_3 , we determine the transition points which we call $\beta_{X/A}$, $\beta_{A/B}$ and $\beta_{B/C}$ for the X - A , A - B and B - C transitions, respectively. For this purpose, it is convenient to investigate $|P_3|$, P_8 and the susceptibilities of them collectively. At $ma = 0.10$, Fig. 6 is obtained as a representative plot where in the upper (lower) panels, left to right, we show Polyakov loop $|P_3|$ (P_8) and its susceptibility as a function of β . Since the data are affected by the finite physical volume, the magnitudes differ from the predictions summarized in Table 1. Nevertheless, from the $|P_3|$ data, we can identify four regions: $\beta \lesssim 5.4$, $5.5 \lesssim \beta \lesssim 5.7$, $5.7 \lesssim \beta \lesssim 6.0$ and $6.0 \lesssim \beta$, as divided by the gray bands. They respectively correspond to the observation of phases X , A , B and C in the distribution plot and we put these labels on the figure. Accordingly, three peaks of $\chi_{|P_3|}$ are seen at $\beta \simeq 5.42$, 5.70 and 6.00 . These locations are consistent with the results in ref. [24]. The peak at 6.00 , where the B - C transition occurs, is milder than the first two as explained in the qualitative discussion of potential barrier in Sec. 4.2.1 for the behavior of $V_{\text{eff}}(\theta_H)$. It is also interesting to see that P_8 becomes zero at the X - A transition ($\beta = 5.42$) and the A - B transition ($\beta = 5.70$). The values at these points change from $-1/8$ to 1 and from 1 to 0 according to the analytical prediction summarized in Table 1. Since, in general, the change of the sign in observables is not affected by lattice artifacts, the zeros of P_8 give a reliable way of locating the transition points. However, this idea is only applicable to the transition where the sign of P_8 changes. Contrary to the analytic prediction, P_8 takes a negative value in the B -phase for reasons which we will discuss later. Therefore, there is no possibility to have another zero around $\beta = 6.0$ for the B - C transition. As seen in the figure, χ_{P_8} is less sensitive to the transitions than others, hence remains in a complementary role.

Results for $ma = 0.05$, 0.50 and 0.80 are shown in Figs. 7, 8 and 9 respectively in the

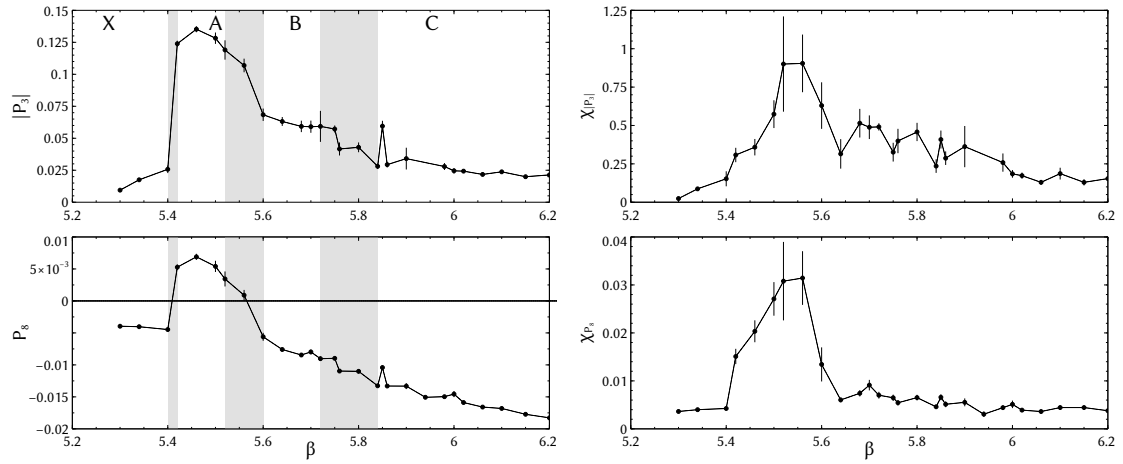


Figure 7. Same figure as Fig. 6 but for $ma = 0.05$.

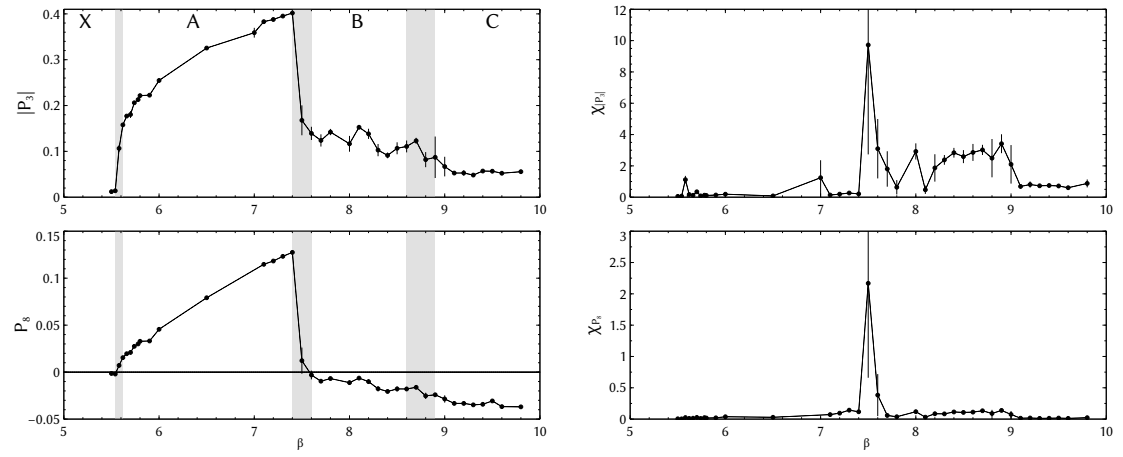


Figure 8. Same figure as Fig. 6 but for $ma = 0.50$.

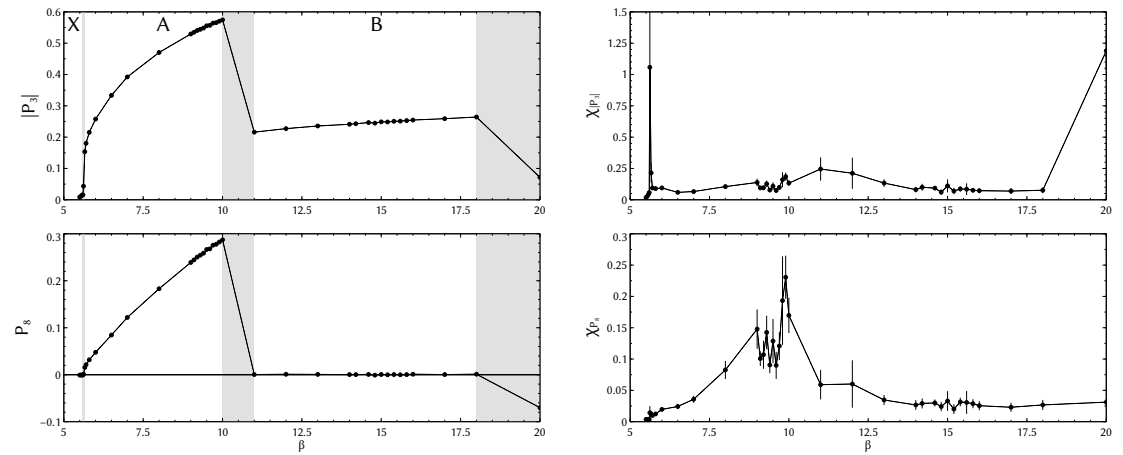


Figure 9. Same figure as Fig. 6 but for $ma = 0.80$.

same organization as in Fig. 6. Again, we label the figure to indicate the corresponding phase observed in the distribution plot of P_3 . For $ma = 0.05$, P_8 becomes zero at values of β consistent with ref. [24]. Looking over P_8 for all bare masses, we see the X - A transition point depends on ma only mildly. This is explained by the fact that the existence of the adjoint fermions does not affect the Z_3 symmetry because the adjoint gauge link is invariant under the associated global Z_3 transformation. On the other hand, for larger ma , the A - B transition occurs at the larger β at which, in the perturbative language, the value of $m_{\text{ad}}R = \hat{m}(\beta) \times N_y/2\pi$ remains in the same level by the running of the renormalized mass $\hat{m}(\beta)$ in the lattice unit. Accordingly, P_8 in the B -phase approaches zero as expected analytically for the perturbative region. In particular, at $ma = 0.80$, P_8 is consistent with zero in the B -phase and the B - C transition is detected at the point where P_8 starts to deviate from zero. However, for such large β value, the physical lattice size is exponentially small. For further discussion on the properties of these transitions, a more detailed study on the finite size scaling has to be done.

With a caveat for the heavy mass region, we summarize the critical values of β for each mass in Table 2. Based on this result, the phase diagram on the β - ma plane is depicted in Fig. 10. In the magnified plot in the inset, we show the approach of the X - A transition point to the confined-deconfined transition point $\beta = 5.692(20)$ (dashed line) for the pure gauge case [42]. Because the B - C transitions are hard to observe clearly from the Polyakov loops or the susceptibilities, we estimate the interval where the transition occurs as follows. The lower boundary of the interval is the highest β where, by inspecting the eigenvalue distribution, we can still clearly identify the B -phase. The upper boundary comes accordingly from the lowest β where we are certainly in the C -phase. Due to the subjective character of the data, we do not quote any error: it is an identification of the region where the transition is occurring.

Table 2. Critical values of β for each ma .

ma	$\beta_{X/A}$	$\beta_{A/B}$	$\beta_{B/C}$
0.05	5.41(1)	5.56(4)	[5.72, 5.84]
0.10	5.42(2)	5.70(4)	[5.95, 6.04]
0.50	5.58(4)	7.50(10)	[8.60, 8.90]
0.80	5.62(4)	10.50(50)	[18.00, 20.00]

5.3 Phase structure with fundamental fermions

We study the dependence of P_3 and P_8 on the boundary phase α_{fd} for several values of β in the presence of fundamental fermions. As explained in Sec. 2.2, we introduce α_{fd} through the boundary condition (2.15). This setup is formally equivalent to finite temperature QCD with an imaginary chemical potential $\nu = \pi + \alpha_{\text{fd}}$. Roberge and Weiss [40] have already shown that the corresponding partition function with $SU(N)$ gauge symmetry is periodic in ν as

$$Z(\nu) = Z(\nu + 2\pi/N) \quad (5.2)$$

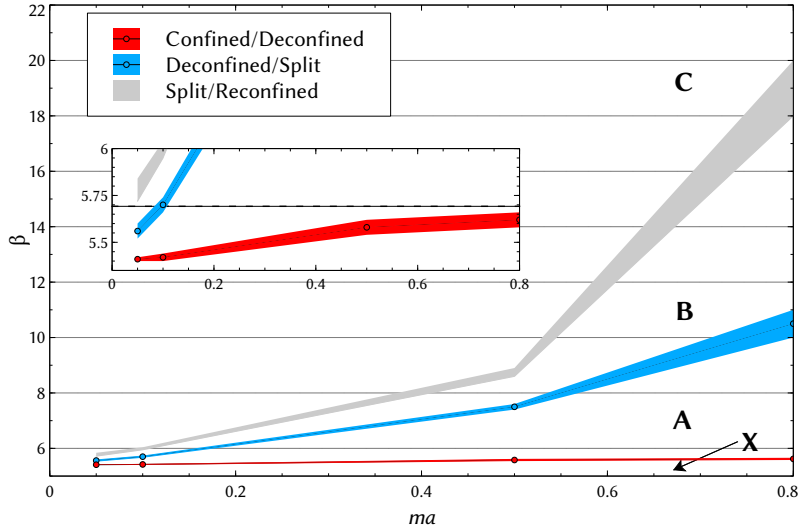


Figure 10. Phase diagram for the $N_{\text{ad}} = 2$ adjoint fermion system with periodic boundary condition in the compact dimension. In the window, the X - A transition line is compared with the pure gauge case (dashed line) [42].

and there are discontinuities (first order lines) at $\nu = 2n\pi/N$ with $n = 0, \dots, N - 1$. These discontinuities exist in a region of high β down to some endpoints which require a non-perturbative study to be located. Several numerical simulations on the lattice, for example [43, 44], have determined these points as well as the phase structure in the $(\beta, \alpha_{\text{fd}})$ plane, *i.e.* the transition lines which were associated with chiral phase transitions and the breaking of the approximate Z_3 symmetry for α_{fd} .

To test our predictions of Section 4, we carry out a numerical simulation with $(N_{\text{ad}}, N_{\text{fd}}) = (0, 4)$. The basic setup is the same as in ref. [44] except for the bare fermion mass being fixed to $ma = 0.10$ in our case. Since we are interested in the symmetries of the Polyakov loop, we determine the locations of the transition points by the peak points of $\chi_{|P_3|}$. Other technical matters related to this simulation are briefly summarized in Appendix B.

We compute the Polyakov loop on the generated gauge configurations in a region of the $(\beta, \alpha_{\text{fd}})$ plane which covers the known phase structure. The resulting distributions of P_3 are shown in Fig. 11 for $\beta = 5.00$ (left), 5.15 (center) and 5.20 (right). In each panel, we cover the range of α_{fd} from 0 to $5\pi/3$. For $\beta = 5.00$, the sizable shift of the data from the origin is caused by the non-zero value of $(ma)^{-1}$, which breaks the Z_3 symmetry. We observe a continuous change of P_3 as a function of α_{fd} in this case. This behavior does not change even at $\beta = 5.15$. On the other hand, the discontinuity of P_3 around $\alpha_{\text{fd}} = 2\pi/3$ is clearly visible for $\beta = 5.20$. In particular, we find that the data at $\alpha_{\text{fd}} = 2\pi/3$ is in the A_1 phase or the A_2 depending on the initial configuration in HMC. This is the indication of the non-analyticity of θ . For a better illustration of this behavior, in Fig. 12, we plot the phase $\arg(P_3)$ as a function of α_{fd} . As seen in the figure, the transition from a continuous behavior to a discontinuous one around $\alpha_{\text{fd}} = 2\pi/3$ becomes more evident for increasing β .

Having confirmed the Roberge-Weiss structure and using the symmetry about $\alpha_{\text{fd}} =$

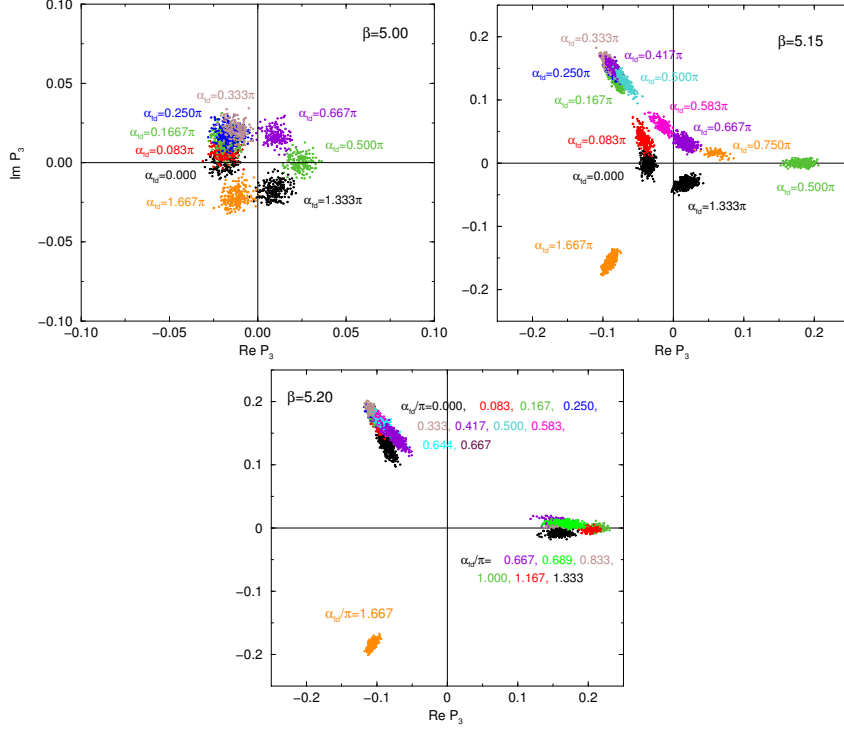


Figure 11. Distributions of P_3 obtained on gauge ensembles with a variation of α_{fd} for $\beta = 5.00$ (left), 5.15 (center) and 5.20 (right). The degrees of α_{fd} used in the calculation are indicated with the corresponding data. Overall, data points with same degrees of α_{fd} are indicated by same colors.

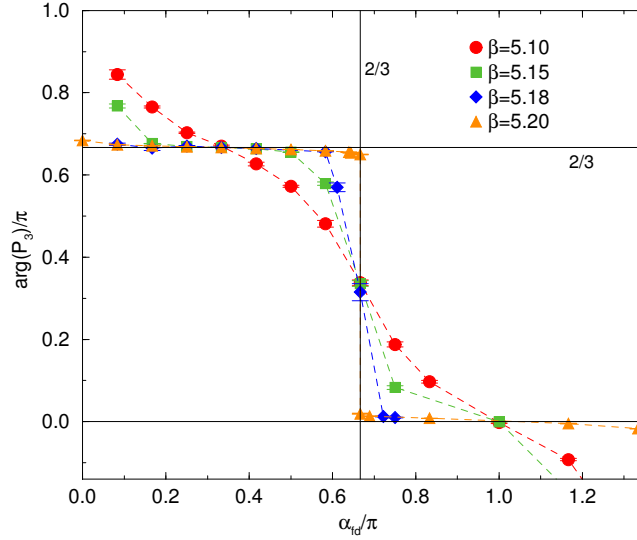


Figure 12. $\arg(P_3)$ as a function of α_{fd} with various values of β .

$\pi/3$, we concentrate on the region $0 \leq \alpha_{fd} < \pi/3$ to determine the A - B (or, confined-deconfined) transition points. For $\alpha_{fd} = n\pi/12$ with $n = 0, 1, 2, 3, 4$, we investigate the susceptibilities of $|P_3|$ and P_3 along with the analysis in the previous section. The upper

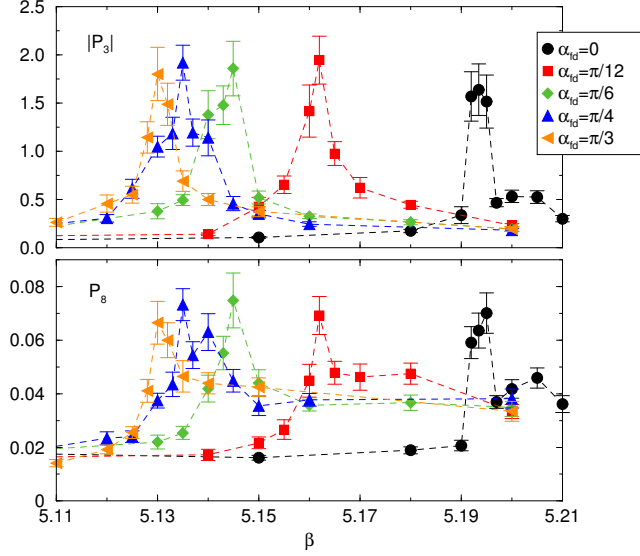


Figure 13. (Left) P_3 as a function of β for various α_{fld} . (Right) The susceptibility of the absolute value of P_3 (upper) and the susceptibility of P_8 (lower) as a function of β for $\alpha = 0, \pi/12, \pi/6, \pi/4, \pi/3$.

and lower panels in Fig. 13 contain plots of $\chi_{|P_3|}$ and χ_{P_8} , respectively. As is expected from the coherence of P_3 and P_8 , we observe the peaks at the same points. From the location of these peaks, we draw the phase diagram in Fig. 14. We note that our data do not differ significantly from the results of ref. [44] with $ma = 0.05$. It suggests that no significant mass dependence of the phase structure is expected. Because the perturbative region is realized at large β , there would be a split of phases into three classes A_1, A_2 and A_3 as described in eq. (4.12) and Figs. 4 and 5.

5.4 Eigenvalues of the Wilson line

In the previous sections, we discussed the existence of different phases looking at values of Polyakov loops and their susceptibilities in the fundamental and adjoint representations. We identify four phases in the case of adjoint fermions with periodic boundary condition. The comparison of the measured values for P_3 and P_8 with the ones listed in Table 1 suggests that they are related to the Hosotani mechanism. In order to clarify the connection of these phases with the perturbative effective potential predictions of Sec. 4.2.1, we show the results of the eigenvalues of the Wilson line wrapping around the compact dimension (cf. eq. (2.4)). These observables are the fundamental degrees of freedom in the perturbative description. We demonstrate that the lattice data match the perturbative results in the weak coupling limit. In the strong coupling region, we show qualitative agreement with the V_{eff} .

On the lattice, the Wilson lines are given by

$$W_3^{\text{latt}}(x) = \prod_{y=1}^{N_y} U_{(x,y),4}, \quad W_8^{\text{latt}}(x) = \prod_{y=1}^{N_y} U_{(x,y),4}^{(8)}. \quad (5.3)$$

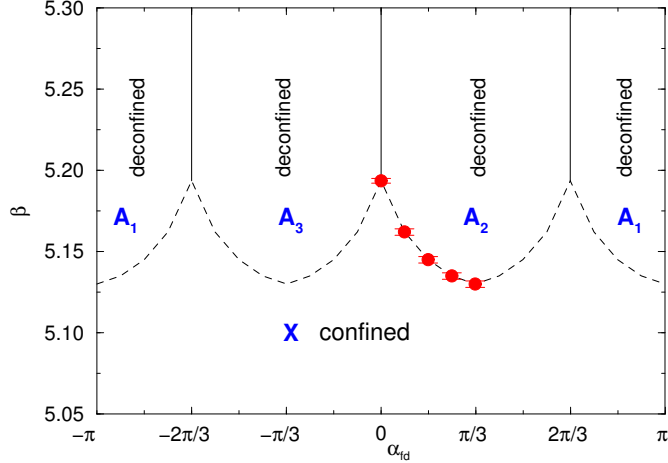


Figure 14. Phase diagram of the $N_{\text{fd}} = 4$ fundamental fermion case. Solid lines indicate discontinuity separating the A phase in the period of $2\pi/3$. Dashed lines are the critical line drawn by connecting the actual data points (red squares) and its copy based on the symmetry and periodicity explained in the text.

The eigenvalues of the Wilson line, eq. (2.6), are independent of the gauge transformations, and their degeneracies classify the pattern of gauge symmetry breaking as explained in Sec. 3. The three complex eigenvalues are denoted by $\lambda = e^{i\theta_1}, e^{i\theta_2}$ and $e^{i\theta_3}$. We constrain each phase within the interval $-\pi \leq \theta_1, \theta_2, \theta_3 \leq \pi$.

5.4.1 Weak coupling regime: fundamental and adjoint fermions

We now consider the agreement of the eigenvalue distribution of the Wilson line with the perturbative prediction in weak coupling regime, $\beta \rightarrow +\infty$ (that implies a compactification radius shrinking to zero), for $N_{\text{fd}} = 4$ fundamental fermions and $N_{\text{ad}} = 2$ adjoint fermions with periodic boundary conditions. In this analysis, the phase differences $\Delta\theta_j = \theta_j - \theta_i$, ($i \neq j$) take a central role. Before showing the lattice results, we summarize the perturbative predictions of $\Delta\theta_j$'s based on the analysis of Sec. 3:

- Fundamental fermions with periodic boundary condition

In this case, the gauge symmetry is never broken. The true vacua of the effective potential are realized at $(\theta_1, \theta_2, \theta_3) = (-\frac{2\pi}{3}, -\frac{2\pi}{3}, -\frac{2\pi}{3})$ or $(\frac{2\pi}{3}, \frac{2\pi}{3}, \frac{2\pi}{3})$, see Fig. 4. In both vacua, the angle of the Wilson line phase ($\Delta\theta_i$) is

$$(\Delta\theta_1, \Delta\theta_2, \Delta\theta_3) = (0, 0, 0). \quad (5.4)$$

- Adjoint fermions with periodic boundary condition

In this case, the $SU(3)$ gauge symmetry is broken to $U(1) \times U(1)$. The true vacua are realized at $(\theta_1, \theta_2, \theta_3) = (0, \frac{2\pi}{3}, -\frac{2\pi}{3})$ and the permutations, thus all eigenvalues of the Wilson line are not degenerate. We expect that

$$(\Delta\theta_1, \Delta\theta_2, \Delta\theta_3) = (\frac{2\pi}{3}, \frac{2\pi}{3}, \frac{4\pi}{3}), \quad (0 \leq \Delta\theta_j < 2\pi) \quad (5.5)$$

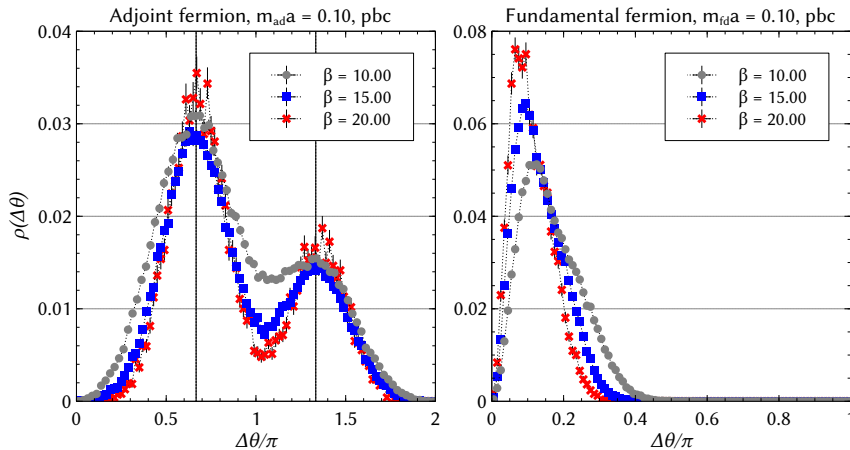


Figure 15. Density plots of $\Delta\theta_i$ ($i = 1, 2, 3$) for $ma = 0.10$ with the periodic boundary condition for adjoint and fundamental fermions, respectively. In the vertical axis the total density fraction is reported. For the readability, in the adjoint fermions case, we draw two lines to identify the expected peak locations $\Delta\theta_i = 2\pi/3$ and $4\pi/3$.

with all possible permutations. In any case the peaks of the distribution are expected at $\pm \frac{2\pi}{3}$.

Figure 15 shows the histograms of $\Delta\theta_1, \Delta\theta_2$ and $\Delta\theta_3$ densities. The left and right panels show the results in the case of adjoint and fundamental fermions, respectively. In both cases, the fermion bare mass is fixed at $ma = 0.10$ and the boundary condition is periodic. We change the value of $\beta = 10.0, 15.0$ and 20.0 .

In the case of the presence of adjoint fermions, the distribution has the expected peaks around $2\pi/3$ and $4\pi/3$ with the ratio 2 to 1 as indicated in (5.5). Furthermore, there is a tendency of the peaks to approach the perturbative values when β becomes high. The higher β corresponds to the smaller lattice spacing, so that the location of peak is expected to remain the same in the continuum limit.

In the case of fundamental fermions we find the positions of the peaks approach $\Delta\theta_i = 0$, which supports the perturbative prediction. However, gauge configurations with $\Delta\theta_i = 0$ have zero probability as the Haar measure for $SU(3)$ [45–47]

$$\prod_{i>j} \sin^2 \frac{\theta_i - \theta_j}{2} \quad (5.6)$$

forbids such configurations. See the density plot in Fig. 16, where the eigenvalue triplets of the Polyakov loop is obtained by random numbers constrained by eq. (5.6). This measure term gives a strong repulsive force for the eigenvalues.

5.4.2 Strong coupling regime: adjoint fermion

Next, we study the most interesting strong coupling region. Here we focus on the presence of adjoint fermions with periodic boundary conditions. In particular, the A, B and C phases should show different degeneracy of eigenvalues.

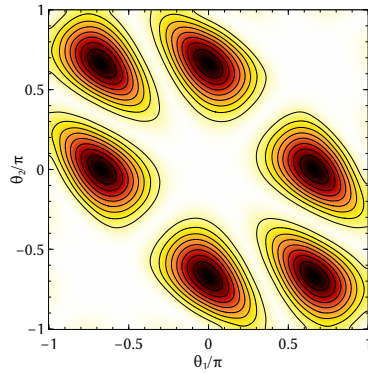


Figure 16. Haar measure density plot. Darker colors denote the highest density regions.

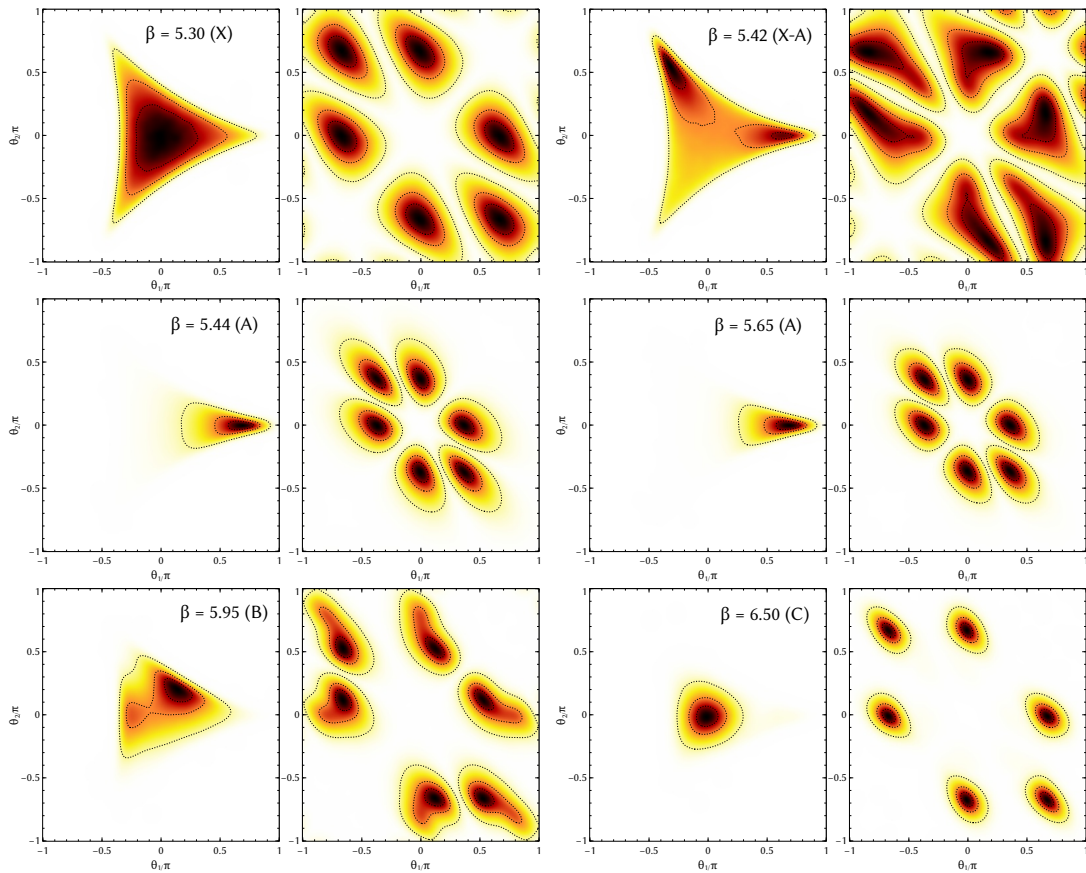


Figure 17. Density plots of the Polyakov loop (in the complex plane) and its eigenvalues (in the $\theta_1/\pi - \theta_2/\pi$ plane) are shown side-by-side at several β 's. All possible pairs $\{(\theta_i, \theta_j), i \neq j\}$ are included in the plots. Darker colors denote the highest density regions.

The results of our investigations are shown in the panels of Fig. 17. These plots come in couples and each one of them displays the density plots for the Polyakov loop P_3 (left) and for the phases (θ_1, θ_2) of its eigenvalues (right). Smearing is applied to the configuration

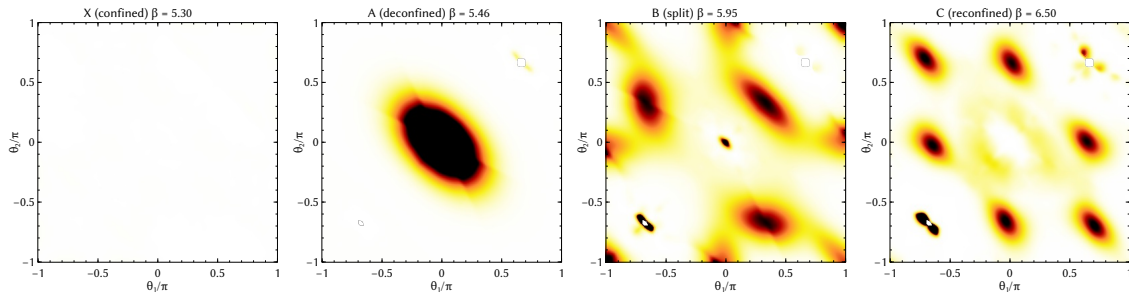


Figure 18. Density plots at several β 's for the Polyakov Loop eigenvalues (in the $\theta_1/\pi - \theta_2/\pi$ plane), as in Fig. 17. Here the original data is divided by the Haar measure distribution. From left to right, the panels correspond to the X , A , B and C phases. The first panel is white as a result of the calculation. Darker colors denote the highest density regions.

before measurements (5 steps of stout smearing [48] with the smearing parameter $\rho = 0.2$) to filter the ultraviolet modes that are essentially just lattice noises and are not relevant for V_{eff} . By this technique, the gauge configuration is smoothed out by averaging the links over the nearest-neighbors, in a gauge invariant way. Several successive steps of smearing can be applied gradually increasing the radius of involved neighbors. The final result is a configuration where the ultraviolet oscillations of the gauge field at the level of the lattice spacing are highly suppressed. It is typically used to clear propagator signals, or obtain information on topological objects. Since we are only interested in locating the minima of the potential, any fluctuations of the Polyakov loop induced by the coarseness of the lattice around that minima is not relevant at this level. We find that smearing is essential to extract useful information from the configurations generated. Data for the 2D histograms are also smoothed by a gaussian filter with a radius of 5 nearest-neighbors for clarity in the presentation. The panels in Fig. 17, from left to right, top to bottom, show the change of distributions in passing the X - A - B - C phases. The eigenvalue densities are not directly comparable with the perturbative prediction seen in Fig. 3 because of the presence of the Haar measure term as explained in the previous subsection. Modulo this contribution, we observe a good correspondence between the perturbative shape of the potential and the location of the maximum of the densities of the measured Polyakov loop eigenvalues.

To strengthen our view, we perform another analysis to eliminate the contribution of the Haar measure seen in Fig. 16 from the density plots. Using the same normalization as the lattice data plots of Fig. 17, it is now easy to isolate the effective potential contribution from the kinetic term of the group measure. The result is plotted in Fig. 18. Although a bit noisy because of the procedure, it shows the expected features of the perturbative potential, and can be directly compared with Fig. 3. The plots, from left to right, are respectively the X , A , B , and C phases ($\beta = 5.30, 5.46, 5.95, 6.50$). The distribution in the X (confined) phase is a constant *i.e.* unity so the plot is a white image, which is a manifestation of a uniform random distribution of the eigenvalues in the two dimensional plane. The A and B phases confirm the conjecture of Fig. 17, *i.e.* that the discrepancy with perturbative prediction is only due to the Haar measure contribution. In the region

around $\theta_1 = \theta_2 = 0, \pm 2\pi/3$, the Haar measure density is close to zero in a wide area and very precise lattice data is needed in order to have a perfect cancellation, so we see some artifacts as a result. An interesting finding is that the C phase shows a completely different behavior from the confined one. The eigenvalues are now not distributed in a random fashion but located in peaks around the Z_3 symmetric values $\theta_i = 0, \pm 2\pi/3$ (again some artifacts appear), with maximal repulsion between them. This regime has been already studied semi-classically in refs. [49, 50]. Removing the gauge group kinetic term from our data, although at the price of introducing some noise, we are able to confirm again the nice agreement of lattice data with the perturbative potential. All the four predicted phases are clearly represented by the data, which is a strong indication of the realization of the Hosotani mechanism in 3+1 dimensions even at the non-perturbative level.

6 Discussions

In this paper we explored the Hosotani mechanism of symmetry breaking in the SU(3) gauge theory on the $16^3 \times 4$ lattice. The Polyakov loop, its eigenvalue phases, and the susceptibility were measured and analyzed in models with periodic adjoint fermions and with fundamental fermions with general boundary conditions. Among the four phases appearing in the SU(3) model with adjoint fermions [24], the A , B , and C phases are interpreted as the SU(3), SU(2) \times U(1), and U(1) \times U(1) phases classified from the location of the global minimum of the effective potential of the AB phases. We confirmed natural correspondence between the effective potential evaluated in perturbation theory on $R^3 \times S^1$ and the distribution of phases of eigenvalues of the Polyakov loop in the lattice simulations. The correspondence was seen in the model with fundamental fermions with varying boundary conditions as well.

The next issue to be settled is the particle spectrum. If the SU(3) symmetry is broken, asymmetry in the particle spectrum must show up in two-point correlation functions of appropriate operators. This can be explored in 4D lattice simulations. It is important from the viewpoint of phenomenological applications. We would like to explain why and how the W and Z bosons become massive in the scheme of the Hosotani mechanism non-perturbatively.

In the end, we would need a five-dimensional simulation to have realistic gauge-Higgs unification models of electroweak interactions. The continuum limit of the 5D lattice gauge theory has been under debate in the literature. Further more, we will need chiral fermions in four dimensions. It is customary to start from gauge theory on orbifolds in phenomenology, however. Lattice gauge theory on orbifolds needs further refinement. We would like to come back to these issues in future.

Acknowledgments

We thank E. Itou for the great contribution in all phases of this work. We would like to thank J. E. Hetrick for his enlightening comment which prompted us to explore the Hosotani mechanism on the lattice. We also thank M. D’Elia and Y. Shimizu for providing helpful information, H. Matsufuru for his help in developing the simulation code, and K. J. Juge

for careful reading of the draft. Numerical simulation was carried out on Hitachi SR16000 at YITP, Kyoto University, and Hitachi SR16000 and IBM System Blue Gene Solution at KEK under its Large-Scale Simulation Program (No. T12-09 and 12/13-23). This work was supported in part by scientific grants from the Ministry of Education and Science, Grants No. 20244028, No. 23104009 and No. 21244036. G. C, E. I and J. N are supported in part by Strategic Programs for Innovative Research (SPIRE) Field 5. H. H is partly supported by NRF Research Grant 2012R1A2A1A01006053 (HH) of the Republic of Korea.

A Useful formulas for $V_{\text{eff}}(\theta)$

We need to evaluate the following building block

$$V(\theta, m) \equiv \frac{1}{2} \sum_{n=-\infty}^{\infty} \int \frac{d^{d-1}p}{(2\pi)^{d-1}} \ln \left[p^2 + \frac{1}{R^2} \left(n + \frac{\theta}{2\pi} \right)^2 + m^2 \right], \quad (\text{A.1})$$

in terms of which V_{eff} is written as in Eq. (4.7). We use the technique of the zeta regularization to write $V(\theta, m) = -\zeta'(0)/2$, where $\zeta(s)$ is the generalized zeta function defined by

$$\begin{aligned} \zeta(s) &= \frac{1}{\Gamma(s)} \sum_{n=-\infty}^{\infty} \int_0^{\infty} dt t^{s-1} \\ &\times \int \frac{d^{d-1}p}{(2\pi)^{d-1}} \exp \left\{ -t \left[p^2 + \frac{1}{R^2} \left(n + \frac{\theta}{2\pi} \right)^2 + m^2 \right] \right\}. \end{aligned} \quad (\text{A.2})$$

Here $\Gamma(s)$ is the Gamma function. Performing integration with p and using Poisson's summation formula,

$$\sum_{n=-\infty}^{\infty} \exp \left[-t \left(\frac{2\pi n + \theta}{2\pi R} \right)^2 \right] = \frac{2\pi R}{\sqrt{4\pi t}} \sum_{\ell=-\infty}^{\infty} \exp \left(-\frac{(2\pi R)^2 \ell^2}{4t} + i\ell\theta \right), \quad (\text{A.3})$$

we obtain

$$\zeta(s) = \frac{\pi^{\frac{d-1}{2}}}{(2\pi)^{d-1} \Gamma(s)} \frac{2\pi R}{\sqrt{4\pi}} \sum_{n=-\infty}^{\infty} e^{in\theta} \int_0^{\infty} dt t^{s-\frac{d}{2}-1} \exp \left[-\frac{(2\pi R)^2 n^2}{4t} - tm^2 \right], \quad (\text{A.4})$$

The $n = 0$ part, though divergent, can be dropped as it is θ -independent.

Using a formula

$$\int_0^{\infty} dt t^{-\nu-1} \exp \left[-tm^2 - \frac{(2\pi R)^2 n^2}{4t} \right] = \frac{2^{1+\nu}}{(2\pi R)^{2\nu} n^{2\nu}} (2\pi R n m)^\nu K_\nu(2\pi R n m), \quad (\text{A.5})$$

and taking $s \rightarrow 0$ limit for $\zeta'(s)$, we obtain

$$V(\theta, m) = -\frac{1}{2^{\frac{d}{2}-1} \pi^{d/2} (2\pi R)^{d-1}} \sum_{n=1}^{\infty} \frac{\cos n\theta - 1}{n^d} \tilde{B}_{d/2}(2\pi R n m). \quad (\text{A.6})$$

where $\tilde{B}_\delta(x) \equiv x^\delta K_\delta(x)$. Normalizing by a factor $\tilde{B}_{d/2}(0) \equiv \lim_{x \rightarrow 0} \tilde{B}_{d/2}(x) = 2^{\frac{d}{2}-1} \Gamma(d/2)$, we finally obtain

$$V(\theta, m) = -\frac{\Gamma(d/2)}{\pi^{d/2}(2\pi R)^{d-1}} \sum_{n=1}^{\infty} \frac{\cos n\theta - 1}{n^d} B_{d/2}(2\pi Rnm) \quad (\text{A.7})$$

which has been used in (4.8).

It would be useful to give another expression of $V(\theta, m)$, which has been obtained in Refs. [51, 52];

$$V(\theta, m) = \frac{1}{\Gamma(\frac{d-1}{2})(4\pi)^{\frac{d-1}{2}} R^{d-1}} \int_{mR}^{\infty} dt t (t^2 - (mR)^2)^{\frac{d-3}{2}} \ln \left[1 + \frac{\sin^2(\theta/2)}{\sinh^2(\pi t)} \right]. \quad (\text{A.8})$$

In both expressions (A.7) and (A.8), the θ -independent constants have been chosen such that $V(0, m) = 0$.

B Lattice technical details

In this section we describe some details of our lattice simulations.

The algorithm to generate the configurations is the Hybrid Monte Carlo (HMC) [37, 38] for both adjoint and fundamental fermions. We obtain a new configuration by N_{MD} steps of evolution of the molecular dynamics trajectory of size $\tau = 1$.

In the case of adjoint fermions, the molecular dynamics integrator is the Omelyan [53] with Hasenbush preconditioning [54]. Using $N_{MD} = 25$ and $\Delta\tau = 0.04$, we obtain an acceptance rate greater than 90%. We accumulate 4,000 - 14,000 trajectories depending on the parameter set (ma, β) . For the fundamental fermions case, by setting $N_{MD} = 50$ and $\Delta\tau = 0.02$ in the standard leapfrog integrator, we obtain acceptance rate $\gtrsim 80\%$. Depending on the value of (β, α_{fd}) , we accumulate 2,500 - 110,000 trajectories depending on the significance of signal.

The observables P_3 and P_8 are computed every 10 generated configurations. For the error analysis, we employ the unbiased jackknife method in both cases. As a reference we report the values of some plaquette values for few values of β and ma in Table 3.

Table 3. Plaquette and $|P_3|$ for some selected β and ma values for reference. Left: adjoint fermion case, Right: fundamental fermion case with $\alpha_{fd} = 0$.

β	ma	plaquette	$ P_3 \times 10^2$	β	ma	plaquette	$ P_3 \times 10^2$
5.30	0.1	0.5087(5)	0.88(4)	4.900	0.1	0.4224(1)	1.73(2)
5.46	0.1	0.5671(1)	13.4(2)	5.000	0.1	0.4433(2)	1.97(3)
5.75	0.1	0.6081(1)	7.9(3)	5.100	0.1	0.4702(4)	2.83(3)
5.95	0.1	0.6279(1)	7.1(4)	5.150	0.1	0.4872(2)	3.71(4)
6.00	0.1	0.6325(1)	6.1(6)	5.180	0.1	0.4997(2)	4.88(5)
6.50	0.1	0.6696(8)	2.6(3)	5.190	0.1	0.5043(3)	5.53(11)
5.50	0.5	0.5272(4)	1.20(8)	5.195	0.1	0.5167(5)	13.52(34)
6.00	0.5	0.6089(2)	25.4(4)	5.200	0.1	0.5203(4)	15.85(10)
7.00	0.5	0.6817(4)	35(1)	5.205	0.1	0.5222(4)	15.87(35)
8.00	0.5	0.7285(7)	11(1)	5.210	0.1	0.5238(5)	16.32(51)
9.00	0.5	0.7617(10)	6(2)	5.220	0.1	0.5269(5)	17.28(53)

References

- [1] Y. Hosotani, *Dynamical Mass Generation by Compact Extra Dimensions*, *Phys.Lett.* **B126** (1983) 309.
- [2] A. Davies and A. McLachlan, *Gauge group breaking by Wilson loops*, *Phys.Lett.* **B200** (1988) 305.
- [3] A. Davies and A. McLachlan, *Congruency class effects in the Hosotani model*, *Nucl.Phys.* **B317** (1989) 237.
- [4] Y. Hosotani, *Dynamics of Nonintegrable Phases and Gauge Symmetry Breaking*, *Annals Phys.* **190** (1989) 233.
- [5] H. Hatanaka, T. Inami, and C. Lim, *The Gauge hierarchy problem and higher dimensional gauge theories*, *Mod.Phys.Lett.* **A13** (1998) 2601–2612, [[hep-th/9805067](#)].
- [6] G. Burdman and Y. Nomura, *Unification of Higgs and gauge fields in five-dimensions*, *Nucl.Phys.* **B656** (2003) 3–22, [[hep-ph/0210257](#)].
- [7] C. Csaki, C. Grojean, and H. Murayama, *Standard model Higgs from higher dimensional gauge fields*, *Phys.Rev.* **D67** (2003) 085012, [[hep-ph/0210133](#)].
- [8] K. Agashe, R. Contino, and A. Pomarol, *The Minimal composite Higgs model*, *Nucl.Phys.* **B719** (2005) 165–187, [[hep-ph/0412089](#)].
- [9] G. Cacciapaglia, C. Csaki, and S. C. Park, *Fully radiative electroweak symmetry breaking*, *JHEP* **0603** (2006) 099, [[hep-ph/0510366](#)].

- [10] A. D. Medina, N. R. Shah, and C. E. Wagner, *Gauge-Higgs Unification and Radiative Electroweak Symmetry Breaking in Warped Extra Dimensions*, *Phys.Rev.* **D76** (2007) 095010, [[arXiv:0706.1281](#)].
- [11] Y. Hosotani and Y. Sakamura, *Anomalous Higgs couplings in the $SO(5)\times U(1)_{B-L}$ gauge-Higgs unification in warped spacetime*, *Prog.Theor.Phys.* **118** (2007) 935–968, [[hep-ph/0703212](#)].
- [12] Y. Adachi, C. Lim, and N. Maru, *Finite anomalous magnetic moment in the gauge-Higgs unification*, *Phys.Rev.* **D76** (2007) 075009, [[arXiv:0707.1735](#)].
- [13] Y. Adachi, C. Lim, and N. Maru, *More on the Finiteness of Anomalous Magnetic Moment in the Gauge-Higgs Unification*, *Phys.Rev.* **D79** (2009) 075018, [[arXiv:0901.2229](#)].
- [14] Y. Adachi, C. Lim, and N. Maru, *Neutron Electric Dipole Moment in the Gauge-Higgs Unification*, *Phys.Rev.* **D80** (2009) 055025, [[arXiv:0905.1022](#)].
- [15] Y. Hosotani, K. Oda, T. Ohnuma, and Y. Sakamura, *Dynamical Electroweak Symmetry Breaking in $SO(5) \times U(1)$ Gauge-Higgs Unification with Top and Bottom Quarks*, *Phys.Rev.* **D78** (2008) 096002, [[arXiv:0806.0480](#)].
- [16] Y. Hosotani, P. Ko, and M. Tanaka, *Stable Higgs Bosons as Cold Dark Matter*, *Phys.Lett.* **B680** (2009) 179–183, [[arXiv:0908.0212](#)].
- [17] N. Haba, Y. Sakamura, and T. Yamashita, *Tree-level unitarity in Gauge-Higgs Unification*, *JHEP* **1003** (2010) 069, [[arXiv:0908.1042](#)].
- [18] Y. Hosotani, S. Noda, and N. Uekusa, *The Electroweak gauge couplings in $SO(5)\times U(1)$ gauge-Higgs unification*, *Prog.Theor.Phys.* **123** (2010) 757–790, [[arXiv:0912.1173](#)].
- [19] Y. Hosotani, M. Tanaka, and N. Uekusa, *Collider signatures of the $SO(5)\times U(1)$ gauge-Higgs unification*, *Phys.Rev.* **D84** (2011) 075014, [[arXiv:1103.6076](#)].
- [20] Y. Adachi, N. Kurahashi, C. Lim, and N. Maru, *$D^0 - \bar{D}^0$ Mixing in Gauge-Higgs Unification*, *JHEP* **1201** (2012) 047, [[arXiv:1103.5980](#)].
- [21] S. Funatsu, H. Hatanaka, Y. Hosotani, Y. Orikasa, and T. Shimotani, *Novel universality and Higgs decay $H \rightarrow \gamma\gamma, gg$ in the $SO(5)\times U(1)$ gauge-Higgs unification*, *Phys.Lett.* **B722** (2013) 94–99, [[arXiv:1301.1744](#)].
- [22] N. Maru and N. Okada, *Diphoton Decay Excess and 125 GeV Higgs Boson in Gauge-Higgs Unification*, *Phys.Rev.* **D87** (2013) 095019, [[arXiv:1303.5810](#)].
- [23] N. Maru and N. Okada, *$H \rightarrow Z\gamma$ in Gauge-Higgs Unification*, *Phys.Rev.* **D88** (2013) 037701, [[arXiv:1307.0291](#)].
- [24] G. Cossu and M. D’Elia, *Finite size phase transitions in QCD with adjoint fermions*, *JHEP* **0907** (2009) 048, [[arXiv:0904.1353](#)].
- [25] M. Unsal and L. G. Yaffe, *Center-stabilized Yang-Mills theory: Confinement and large N volume independence*, *Phys.Rev.* **D78** (2008) 065035, [[arXiv:0803.0344](#)].
- [26] Y. Hosotani, *Gauge-Higgs Unification Approach*, *AIP Conf.Proc.* **1467** (2012) 208–213, [[arXiv:1206.0552](#)].
- [27] K. Kashiwa and T. Misumi, *Phase structure and Hosotani mechanism in gauge theories with compact dimensions revisited*, *JHEP* **1305** (2013) 042, [[arXiv:1302.2196](#)].
- [28] N. Irges and F. Knechtli, *Lattice gauge theory approach to spontaneous symmetry breaking from an extra dimension*, *Nucl.Phys.* **B775** (2007) 283–311, [[hep-lat/0609045](#)].

- [29] N. Irges and F. Knechtli, *Mean-Field Gauge Interactions in Five Dimensions I. The Torus*, *Nucl.Phys.* **B822** (2009) 1–44, [[arXiv:0905.2757](#)].
- [30] P. de Forcrand, A. Kurkela, and M. Panero, *The phase diagram of Yang-Mills theory with a compact extra dimension*, *JHEP* **1006** (2010) 050, [[arXiv:1003.4643](#)].
- [31] L. Del Debbio, A. Hart, and E. Rinaldi, *Light scalars in strongly-coupled extra-dimensional theories*, *JHEP* **1207** (2012) 178, [[arXiv:1203.2116](#)].
- [32] N. Irges, F. Knechtli, and K. Yoneyama, *Mean-Field Gauge Interactions in Five Dimensions II. The Orbifold*, *Nucl.Phys.* **B865** (2012) 541–567, [[arXiv:1206.4907](#)].
- [33] N. Irges, F. Knechtli, and K. Yoneyama, *Higgs mechanism near the 5d bulk phase transition*, *Phys.Lett.* **B722** (2013) 378–383, [[arXiv:1212.5514](#)].
- [34] H. Hatanaka, *Matter representations and gauge symmetry breaking via compactified space*, *Prog.Theor.Phys.* **102** (1999) 407–418, [[hep-th/9905100](#)].
- [35] Y. Hosotani, *Dynamical gauge symmetry breaking by Wilson lines in the electroweak theory*, *Proceedings of SCGT2004* (2005) 17–34, [[hep-ph/0504272](#)].
- [36] C. Gattringer and C. B. Lang, *Quantum chromodynamics on the lattice*, *Lect.Notes Phys.* **788** (2010) 1–343.
- [37] S. Duane, A. Kennedy, B. Pendleton, and D. Roweth, *Hybrid Monte Carlo*, *Phys.Lett.* **B195** (1987) 216–222.
- [38] S. A. Gottlieb, W. Liu, D. Toussaint, R. Renken, and R. Sugar, *Hybrid Molecular Dynamics Algorithms for the Numerical Simulation of Quantum Chromodynamics*, *Phys.Rev.* **D35** (1987) 2531–2542.
- [39] J. Kogut and L. Susskind, *Hamiltonian formulation of Wilson’s lattice gauge theories*, *Phys. Rev. D* **11** (Jan, 1975) 395–408.
- [40] A. Roberge and N. Weiss, *Gauge theories with imaginary chemical potential and the phases of QCD*, *Nucl.Phys.* **B275** (1986) 734.
- [41] F. Karsch and M. Lutgemeier, *Deconfinement and chiral symmetry restoration in an $SU(3)$ gauge theory with adjoint fermions*, *Nucl.Phys.* **B550** (1999) 449–464, [[hep-lat/9812023](#)].
- [42] M. Fukugita, M. Okawa, and A. Ukawa, *Order of the deconfining phase transition in $SU(3)$ lattice gauge theory*, *Phys.Rev.Lett.* **63** (1989) 1768.
- [43] P. de Forcrand and O. Philipsen, *The QCD phase diagram for small densities from imaginary chemical potential*, *Nucl.Phys.* **B642** (2002) 290–306, [[hep-lat/0205016](#)].
- [44] M. D’Elia and M.-P. Lombardo, *Finite density QCD via imaginary chemical potential*, *Phys.Rev.* **D67** (2003) 014505, [[hep-lat/0209146](#)].
- [45] D. J. Gross, R. D. Pisarski, and L. G. Yaffe, *QCD and Instantons at Finite Temperature*, *Rev.Mod.Phys.* **53** (1981) 43.
- [46] N. Weiss, *The Wilson Line in Finite Temperature Gauge Theories*, *Phys.Rev.* **D25** (1982) 2667.
- [47] F. Bruckmann, *A random matrix-like model for the Polyakov loop and center symmetry*, *arXiv:1007.4052 [hep-ph]* (2010) [[arXiv:1007.4052](#)].
- [48] C. Morningstar and M. J. Peardon, *Analytic smearing of $SU(3)$ link variables in lattice QCD*, *Phys.Rev.* **D69** (2004) 054501, [[hep-lat/0311018](#)].

- [49] E. Poppitz, T. Schäfer, and M. Ünsal, *Universal mechanism of (semi-classical) deconfinement and theta-dependence for all simple groups*, *JHEP* **1303** (2013) 087, [[arXiv:1212.1238](#)].
- [50] M. M. Anber and M. Ünsal, *QCD in magnetic field, Landau levels and double-life of unbroken center-symmetry*, *to appear* (2013).
- [51] H. Hatanaka and Y. Hosotani, *SUSY breaking scales in the gauge-Higgs unification*, *Phys.Lett.* **B713** (2012) 481–484, [[arXiv:1111.3756](#)].
- [52] A. Falkowski, *About the holographic pseudo-Goldstone boson*, *Phys.Rev.* **D75** (2007) 025017, [[hep-ph/0610336](#)].
- [53] I. P. Omelyan, I. M. Mryglod, and R. Folk, *Optimized verlet-like algorithms for molecular dynamics simulations*, *Phys. Rev. E* **65** (May, 2002) 056706.
- [54] M. Hasenbusch, *Speeding up the hybrid Monte Carlo algorithm for dynamical fermions*, *Phys.Lett.* **B519** (2001) 177–182, [[hep-lat/0107019](#)].